Departament d'Enginyeria Mecànica

UNIVERSITAT POLITÈCNICA DE CATALUNYA

DEPARTMENT OF MACHINE ELEMENTS AND TRIBOLOGY

NATIONAL UNIVERSITY OF SCIENCE AND TECHNOLOGY

POLITEHNICA BUCHAREST, ROMANIA

Fractal approach to wheel-rail roughness contact theory

by

Laura Maria BABICI

Thesis submitted to obtain the title of

Doctor in Mechanical Engineering

by the

Universitat Politècnica de Catalunya (UPC)

and

National University of Science and Technology

Politehnica Bucharest, Romania (UPB)

December 2023

Acknowledgements

The completion of this research work would not have been possible without the help and support of several individuals to whom I wish to express my deepest gratitude.

I would like to extend my deepest gratitude to my supervisors, Prof. Jordi Romeu and Prof. Andrei Tudor, for their guidance, continuous support throughout my Ph.D. studies, and for their patience, motivation, and vast knowledge. Their counselling has been instrumental throughout the period of research and writing of this thesis. Their tireless efforts in shaping my scientific thought and in enhancing the clarity and depth of my analysis deserve special recognition.

My sincere gratitude also goes to Dr. Cristian Ulianov, who provided me with the opportunity to join their Railway Technology Team Lead as a visiting researcher at Newcastle University, UK, offering me fresh perspectives in my research and helping me to broaden my horizons in this field of study.

I sincerely thank the leadership of the Romanian Railway Authority, the Faurei Railway Testing Center in Romania, and the leadership of Softronic Craiova, which significantly contributed by providing the essential experimental facilities for this study. I would like to thank the leadership and colleagues of the Romanian Railway Authority, specifically the Railway Notified Body Directorate - Laboratories Department, for all their support and understanding, making the completion of my thesis possible.

Furthermore, I would like to express my appreciation, especially to prof. Robert Arcos, to all members of the LEAM research group at UPC and the Department of Machine Elements and Tribology at UPB. This research would not have been accomplished without their valuable opinions and ideas.

I would like to extend my heartfelt thanks to the review and guidance committee from the Department of Machine Elements and Tribology at UPB, comprised of prof. Filip Ilie, prof. Alexandru Radulescu, and prof. Adrian Predescu, for their unwavering support and valuable suggestions that have significantly contributed to the refinement and success of this research. I am also very grateful to all my colleagues at LEAM and the Department of Tribology for their friendship and assistance.

Finally, and most importantly, I wish to thank my husband, son, and entire family. Their support has gone beyond mere encouragement, being a constant source of comfort and emotional stability. Their role in this academic journey has been as vital as any academic contribution, providing me with the balance and well-being necessary to continue this pursuit of knowledge.

Contents

The thesis contains 123 pages, 18 tables, 40 figures, an annexe and 180 bibliographic sources. In this summary, the numbering of equations, tables, and figures corresponds to that used in the full thesis.

Chapter 1

Introduction

This chapter introduces the current thesis, beginning with a concise overview of harmonised legislation concerning wheel-rail roughness and its implications for rolling noise. Following that, an explanation is provided for adopting a simulated fractal approach, which targets the prediction of rail roughness and static friction coefficients. Within the Hertzian contact experiments, the acoustic emissions arising from the relative movement of the cylinder-plane specimens served as indicators for the onset of the slip phase, thereby establishing themselves as essential non-destructive tools in detecting and monitoring the slip phenomenon while concurrently accompanying the friction process. The experimental findings assertively corroborated that friction coefficient variations and bursts of acoustic emission are congruent across all contact pressure conditions and sliding velocities. After presenting the justification, the primary goals of the thesis are outlined. The chapter then culminates with a brief overview of the topics covered in each subsequent thesis section.

1.1.   Overview

In the context of the ongoing modernisation of the European railway infrastructure, the compliance of rolling stock with current technical regulations is essential to ensure interoperability and reduce noise pollution. European standards, notably the "Technical Specifications for Interoperability" (TSI), as well as Directive 2008/57/EC and Regulation (EU) No. 1304/2014 of 26 November 2014, underscore the necessity for this compliance, aiming to guarantee the compatibility of vehicles within the EU territory and mitigate railway noise. A particular emphasis is placed on the identification and control of the main sources of noise. In the railway sector, it is unequivocally recognised that the intricate wheel-rail interaction primarily causes rolling noise. Both components' roughness and mutual engagement significantly influence this interaction and the resulting noise.

Thus, the roughness of the rail in the contact between the rail and the wheel significantly impacts the microstructural interaction, directly impacting the running noise (*Thompson, 2003, R.J. Diehl, P. Holm, 2006, Wu, 2006*). When a wheel moves over a rail with variable roughness, the interaction can generate noise fluctuations due to the variation in contact intensity and intermittent contact. This phenomenon can lead to increased noise, with considerable potential for noise pollution

in the areas adjacent to the railway. Moreover, roughness directly influences the transmission of forces through the wheel-rail system, generating oscillations or vertical vibrations that affect both the passenger's comfort and the lifespan of components and infrastructure (*R. Arcos, 2011, E. Verheijen, 2006*). In addition to these immediate effects, roughness plays a key role in determining wear and maintenance needs. A rough rail can cause uneven wear, both in the wheel and in the rail, resulting in increased costs and the need for more frequent repairs. The adhesion between the wheel and the rail can also be compromised due to roughness, affecting the acceleration and braking efficiency of the train and, implicitly, the safety and overall performance (*Zhang, 2002*). In addition, roughness-induced vibrations can be transferred to neighbouring structures and soil, creating the potential for discomfort in nearby communities and affecting adjacent structures. For all these reasons, it is clear that monitoring and managing rail roughness is crucial for efficient and safe rail transport.

In the study of surface roughness and Hertzian contact mechanics, the fractal method presents an alternative approach. Fractals, structures or patterns that replicate across multiple scales highlight the auto-similar nature observed in many natural phenomena, including surface roughness.

Through these fractal structures, it becomes possible to represent the complexity of roughness from macroscopic features down to microscopic asperities more effectively than with traditional methods. Furthermore, due to their inherent auto-similar and auto-affine properties, fractals ensure a consistent roughness representation, maintaining the overall contour regardless of the scale at which it is analysed.

Utilising the Weierstrass-Mandelbrot function, the fractal method employs geometric progressions to model and simulate the subtle variations in roughness. This approach provides specific parameters for roughness characterisation that are independent of the resolution of the instrument, thereby facilitating a consistent roughness simulation across various scales.

In contrast to the traditional method, where the analysis of roughness is limited by the resolution of the instruments used, the fractal method proves to be versatile, accommodating changes observed at every scale. This attribute grants fractals a distinct advantage in terms of adaptability and comprehensive analysis of surfaces when compared to conventional methods.

The coefficient of friction in rail transport is important due to its influence on the interactions between the surfaces in contact, such as establishing the capacity to accelerate, brake or navigate safely. It also characterises the degree of adhesion or slip between two surfaces in relative motion and can determine the behaviour of a system in situations of braking, traction or slipping. The adequate value of the COF ensures the efficient transmission of forces from wheel to rail, allowing adequate traction and avoiding unwanted phenomena, such as wheel skating or accelerated wear. COF also influences rail and wheel wear rates, directly impacting the maintenance costs and life of the railway infrastructure. Unforeseen variability or changes in COF may result in loss of adhesion, causing

possible skidding or slipping, with associated risks of accidents or material damage. In addition, properly managing the coefficient of friction helps prevent premature wear of components, reducing maintenance costs and extending the life of the infrastructure.

The "stick-slip" phenomenon in the railway system dynamics manifests rapid and distinct transitions between the adhesion and sliding phases of the wheel-rail Hertzian contact, stemming from variations in the friction coefficient, changes in humidity conditions, and the presence of contaminants at the contact interface. This behaviour, influenced by mechanical and environmental factors, can induce vibrations in the rolling stock and railway infrastructure, leading to acoustic emissions, often referred to as rolling noise, with the potential to disrupt the comfort of passengers and adjacent communities to railway lines. In this context, acoustic emissions (AE) are high-precision, non-destructive tools, allowing the observation and analysis of the stick-slip phenomenon, especially by clearly delineating the onset of the slip phase. Furthermore, the alternation between adhesion and sliding, precisely the stick-slip phenomenon, can accelerate wear processes at the wheel and rail level, significantly reducing the lifespan of components, increasing operational and maintenance costs and, under certain circumstances, compromising travel safety, generating speed fluctuations and potential skidding. Such fluctuations can also alter the train's rolling performance, thereby affecting the overall efficiency of railway transport. Within the framework of maintaining the integrity and optimal functioning of the railway system, modern approaches, such as monitoring and adjusting the static friction coefficient through fractal modelling, are promoted as innovative solutions for managing and mitigating the impact of the stick-slip phenomenon, simultaneously ensuring efficient predictive maintenance.

1.2. Motivations

Monitoring and quality control of the railway track by evaluating the measured roughness is imperative in assessing the operation state. Although roughness is often perceived only as a physical characteristic, it plays a significant role as a source of rolling noise, having major implications on efficiency, safety, and environmental compliance. Given the multifaceted nature of roughness and its non-uniform manifestation across different scales, the fractal approach offers a more comprehensive analysis. Utilising fractal methods enables a deeper understanding of the intricate patterns and self-similarities inherent in roughness, which traditional methods might overlook. This enhanced insight gained through fractal analysis allows for more precise diagnostics, prediction, and mitigation strategies, ultimately leading to better management of the associated challenges posed by rolling noise and the ensuing impacts on railway operations.

The traditional modelling of Hertzian contact, based on the interaction between wheel and rail considering roughness, does not always accurately illustrate the complex interface interactions. With the introduction of fractal theory, a new perspective is opened on the true nature of the contact area

between the wheel and rail. Opting for fractal theory in contact mechanics provides a much more detailed view, taking into account the inherent complexities and variations at different scales present in the contact surfaces of the real world.

By approaching this perspective, one can arrive at a more accurate representation and prediction of Hertzian contact behaviour, thus creating more efficient solutions for reducing wear, decreasing noise, and optimising performance in railway systems. This justifies the need for detailed research in this field, as a deep understanding of these interactions can lead to significant innovations in railway engineering and overall infrastructure improvement.

The "stick-slip" phenomenon, characterised by a swift transition between adhesion and sliding, has profound implications in the railway domain, impacting performance and operational safety. A deep understanding of this phenomenon within contact mechanics allows us to identify and analyse the root causes of its manifestation and how it can influence the overall system behaviour. With this foundation of knowledge, effective solutions can be developed to minimise or eliminate the adverse impact of stick-slip, offering the opportunity to enhance the quality and efficiency of system operation. By delving deeper into the study of this phenomenon in the realm of contact mechanics, we can reveal the subtle details and complexities of the interaction, thus facilitating the development of more advanced monitoring, control, and optimisation strategies.

1.3.   Thesis objectives

The primary objective of this research is to develop and implement specific algorithms based on fractal techniques for studying roughness within contact mechanics. Particular attention is given to investigating the roughness of railway wheels and tracks to provide essential information for the efficient maintenance of railway components and for mitigating vibrations and rolling noise.

The following task have been undertaken:

- Modelling roughness using the fractal formulation, based on the detailed analysis of 41 roughness parameters obtained from experimental measurements; to achieve this goal, the Weierstrass-Mandelbrot (W-M) function was applied to the mentioned parameters, and the results thus obtained were then compared with the original data to verify the validity of the fractal method, placing particular emphasis on acoustic roughness modelling, under the standards set by EN ISO 15610:2019.

- Modelling roughness through the fractal formulation, encompassing contact mechanics parameters and explicitly addressing the static coefficient of friction (COF), provides a nuanced understanding of surface interactions at varying scales. This method makes capturing the multifaceted nature of wheel-rail contact interactions feasible, which often eludes traditional modelling techniques. Such an approach not only refines our grasp of the

underlying mechanisms but also paves the way for enhanced predictive capabilities, aiding in designing and maintaining more efficient systems in railway engineering contexts.

- Analysing the stick-slip behaviour in a Hertzian contact involves investigating the correlations between Acoustic Emission (AE) minimal parameters and the COF (coefficient of friction), particularly at low and very low driving speeds. The initiation of relative motion between two bodies in friction is foundational in understanding the principle of friction in tribology. Through this approach, the minimal AE parameters prove to be both adequate and sufficient to detect and monitor the stick-slip phenomenon, pinpointing the onset of the slip phase. This establishes AE as an effective, non-destructive tool for detecting and monitoring the stick-slip behaviour.

- Validation of the friction static coefficient using the fractals method and its comparison with the experimental static friction coefficient results.

1.4. Thesis Outline

The content of the present thesis is divided into five chapters. All chapters except Chapter 1 and Chapter 5, Introduction and Conclusion, and Further Work, respectively, include their state-of-the-art within the introduction. The chapters of the thesis are organised as follows:

Chapter 1 presents a general introduction to the research, the justifications, the objective and the thesis outline.

Chapter 2 introduces a methodology that employs fractal modelling techniques to capture rail roughness characteristics intricately. The complex nature of rail roughness is depicted in detail by using both the structure and Weierstrass Mandelbrot functions. Data from the Făurei Railway Testing Centre in Romania validate that the roughness height exhibits distinct mathematical fractal traits. A total of 41 classical statistical parameters derived from roughness measurements were juxtaposed against their simulated fractal counterparts. Parameters such as the Autocorrelation function, Amplitude Density Function, Bearing Area Curves, and rail acoustic roughness were generated using the Weierstrass function. Comparisons between these parameters and the actual measured data indicate significant congruence. Most parameters demonstrated a relative error within a 10% range, emphasising the effectiveness of the fractal approach in assessing rail roughness dynamics. Consequently, the simulated parameters could be vital tools for rail roughness evaluation, promoting enhanced track maintenance, grinding, and noise reduction.

Chapter 3 focuses on the analysis of the static coefficient of friction (COF) and Hertzian contact parameters from a fractal perspective. This approach enables the fractal model to encompass the real contact area, reflecting the surface asperities not as ideal geometric shapes but as complex and irregular structures, which more accurately represent reality. This significantly enhances

understanding of phenomena within the contact zone and contributes to more accurate modelling of contact parameters.

The work highlights that the COF value is affected by the material characteristics of rough surfaces, the fractal parameters describing the topography, and the applied normal force. The fractal model, with its ability to simulate complex interactions at a micrometric scale, provides a valuable contribution to predicting and analysing contact behaviour. Thus, it paves the way for advanced design and optimisation of mechanical systems, with direct applications in areas where friction and wear determine performance and reliability, such as in the railway industry.

Based on the WM model, four deformation regimes have been assessed: elastic, the first and second elastoplastic, and fully plastic. The static friction coefficient, theoretically derived from fractals and contact mechanics, can be viewed as the "intrinsic property" of the softer of the two entities in contact, marked by its surface microgeometry in terms of fractal dimensions. This approach to contact mechanics within the fractal context paves the way for advancing more robust methods for managing and controlling adherence under diverse operating conditions.

Chapter 4 highlights that the fundamental AE parameters effectively detect the stick-slip phenomenon. Using a custom configuration of the tribometer tailored for these experiments, a thorough analysis of AE signals was conducted, bypassing the need for traditional AE equipment. The central aim of the tests was to delve into the interrelations between AE and COF parameters, emphasising extremely low driving speeds, considering the onset of relative movement between two frictional bodies is key to grasping the friction principle in tribology.

In this context, connections were established between foundational AE characteristics and stick-slip attributes, like static and kinetic friction coefficients, as well as their temporal evolution. Tribological tests were carried out on the cylinder-plane specimen under dry friction conditions at varied Hertzian contact pressures and driving speeds. The rig was set to record AE, normal, and frictional forces concurrently, noting that AE peaks followed immediate variations in the friction coefficient. Findings revealed the sensitivity of AE amplitude and energy to the stick-slip manifestation, with energy profiles for both AE and COF indicating consistent patterns based on driving speed. Ultimately, the fractal-derived static friction coefficient was compared to the experimentally obtained coefficient at a driving speed of zero.

Chapter 2

Fractal - based modelling of rail roughness

2.1.   Introduction

The primary aim of this chapter is to examine the fractal nature of rail surface roughness, which is based on roughness measurements taken at the Făurei Railway Testing Centre (TCF) in Romania, by deriving the fractal parameters and defining two essential parameters, *D* and G_f, to characterise the rail roughness accurately. To achieve this goal, an evaluation and a comparison of the classical statistical parameters obtained from roughness measurements with simulated fractal parameters was performed using the WM function for the same measurements.

In addition, acoustic roughness modelling was performed using the WM function and the results were compared with the acoustic roughness data obtained from the experimental measurements. By comparing the classical statistical parameters with the fractal parameters obtained from the WM function and analysing the acoustic roughness data, the paper seeks to offer an in-depth insight into the fractal characteristics of the roughness of the rail surface.

2.2.   Theory

For a signal $y_r(x)$, whose increment $y_r(x_i + \tau) - y_r(x_i)$ is assumed to have a Gaussian distribution with zero mean, a function called a structure-function (SF) in continuous forms (*P. R. Nayak, 1973*) is defined:

$$SF(\tau) = \langle (yr(x) - yr(x + \tau))^2 \rangle = C_t(|\tau|)^{(4-2D)}, \tag{2.1}$$

where τ is a displacement along the x-axis $C_t = \psi G_f^{2(D-1)}$, *D* and G_f are the fractal parameters, and Ψ *(A G.Y. Zhou et al., 1993)* is given by the equation:

$$\psi = \frac{\Gamma(2D-3)\,sin(2D-3)\pi/2}{2-D}, \tag{2.2}$$

in which Γ ( ) represents the Gamma function.

The graph of S(τ) concerning τ in Eq. (1) appears as a straight line when plotted using double logarithmic coordinates of the form:

$$log(S(\tau)) = (4 - 2D)\,log\,\tau + log\,C_t, \tag{2.3}$$

If the original signal *yr (x)* is divided into *Nr* equal intervals, $\Delta x = x_q/Nr$, where x_q is the length of the measured section, the SF in discrete form, *SF(k),* of a signal $yr(x_i)$ is:

$$SF(k) = \frac{1}{Nr-k}\sum_{i=1}^{Nr-k}(yr_{i+k} - yr_i)^2, \tag{2.4}$$

where, *SF(k)* represents the SF in discrete form and *k* varies in the range 1 to *Nr*.

Once D and G_f are known, the roughness can be estimated using fractal parameters by the WM continuous function $yrW(x)$ of the following form (*Majumdar A. and Bhushan B., 1990, Mandelbrot B. B., 2021, Zhang X., Xu Y. and Jackson R. L., 2017, Majumdar A., Tien C. L., 1991, Singh A. N., 1953, Green I., 2020*):

$$yrW(x) = G_f^{D-1} \sum_{n=nl}^{nh} \frac{cos(2\pi\gamma^n x)}{\gamma^{(2-D)n}}, \qquad 1< \gamma <2 \qquad (2.5)$$

where, *yrW(x)* represents the height of the generated fractal profile, and G_f is the characteristic length scaling constant *(Zhou A. G. Y. et al., 1993)*; it establishes the position of the spectrum on the power axis and remains unchanged concerning all roughness frequencies; D represents the fractal dimension of the profile, and it can be a non-integer value between 1 and 2 for 2D and between 2 and 3 for 3D; γ is a parameter which determines the frequency density in the roughness analysis; n is the integer number of items gathered by the series during the roughness measurement process, and it indicates the total number of data points considered in the analysis; nh corresponds to the high cut-off frequency of the profile, depending on the resolution of the instrument used to capture the roughness data, and nl corresponds to the low cut-off frequency of the profile. By setting appropriate values for γ, n, nh, and nl, we can control the frequency range of the roughness data used in the analysis.

2.3.   *Methodology*

This study aimed to establish a correlation and comparative analysis between rail roughness parameters obtained through experimental measurements conducted at Făurei Railway Testing Centre, Romania, and those derived from simulated roughness profiles generated using the fractal method involving the WM function.

This comparison helps validate the effectiveness of the fractal method in capturing the essential characteristics of roughness and provides valuable information related to noise generation and track maintenance. Also, the rail roughness was predicted using the fractal model with the Weierstrass function.

The method of measuring direct rail acoustic roughness involves placing the transducer on the surface of the rail, which allows an isolated measurement of the roughness of the rail without being influenced by wheel surface roughness or other potential interactions of wheel-rail contact. The rail acoustic roughness was compared with the rail acoustic roughness calculated using the fractal method involving the WM function.

2.3.1.   *Experimental measurements*

The experimental tests were carried out within the Făurei Railway Testing Centre, belonging to the Romanian Railway Authority.

To determine the roughness of the track on the Big Ring, a segment of straight-line type UIC 60 was chosen, on ballast bed and concrete sleepers, without visible joints or defects, located at kilometre marker 6 + 900 km (Figs. 2.1-2.2).

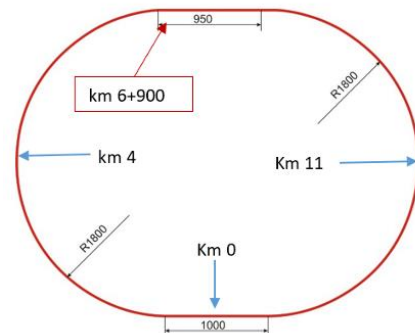Fig. 2.1. RailwayTesting Centre
Graphic presentation.

Fig. 2.2. Testing area.

The tests were conducted following the guidelines outlined in EN 15610:2019 (Chapter 5), employing the direct approach for measuring rail surface roughness. A total test surface length of 30 m was considered, comprising four test sections of 7.5 m each. These four test sections with the roughness measured on the centreline of the surface were analysed. The rail roughness measurements were performed using a high-precision measuring system m|rail trolley equipment, that uses an interdependent acceleration sensor that is manually moved along the rail (trolley) and continuously records the rail roughness with a vertical resolution of 1 mm.

2.3.2. *Data processing of roughness*

In order to analyse the rail roughness condition, the experimental sequence of the roughness profile of centre line vector *yr(x_i)* for the centre-hand thread of the outer ring of length 7.5 with a profile discretisation of 1 mm was selected and analysed. The peak removal techniques and curvature processing were performed for roughness data, according to EN 15610:2019, chapter 5.

In order to eliminate the effects of dust or dirt granules on the rail head, an algorithm has been included that removes "spikes and pits", i. e. very short spikes and pits (much reduced than the wheel-rail contact area). A second algorithm, known as "curvature processing," is developed to manage similar features that the small radius tip of the probe would detect but would not affect a much larger radius wheel.

2.3.3. *Calculations*

Different surface roughness parameters are compared to check if the fractal approach is suitable to model roughness. Thus, 41 parameters defined as amplitude, spatial and hybrid parameters

calculated in 2D (*Majumdar A., Bhushan B., 1991*) and the rail acoustic roughness were analysed. In order to compare the experimentally determined roughness with the simulated roughness obtained by the WM method, the roughness parameters for the four measured test sections of 7.5 m each were compared.

2.4. Results and discussions

The *SF* analysis method was employed to examine the fractal nature of the rail roughness from CTF Făurei Romania and to determine the fractal parameters for each segment of roughness-subjected analysis following Eqs. 2.1-2.4. This analysis confirmed the fractal nature of the rail's roughness as each segment adhered to the exponential law criterion, indicated by its linear behaviour on a double logarithmic scale in the structure-function plot (Fig. 2.4.a). Following the fractal method, which used the WM function and involved the fractal dimension, D, the characteristic length scaling constant G_f, and other relevant parameters, synthetic roughness profiles were created to mimic the fractal nature of the real roughness of the rail. The fractal roughness simulated by WM modelling and the measured roughness for the first section of the length of 7.5 m is shown in Fig. 2.4.b, and it can be seen that simulated roughness follows the same trend as measured roughness.
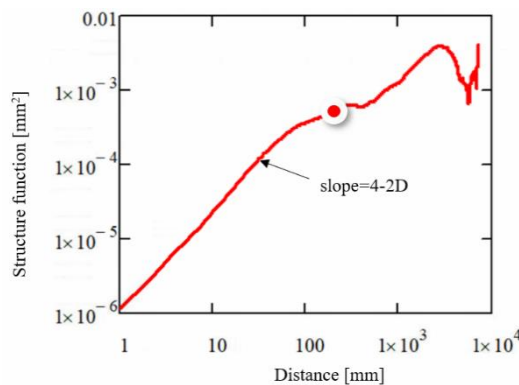

Fig. 2.4.a. Structure-function log-log of the rail roughness measurement data (7.5 m).
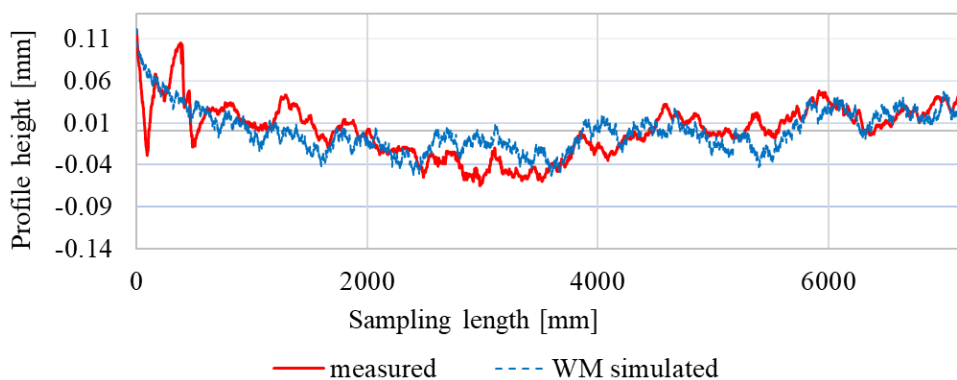

Fig. 2.4.b. Comparison between experimental (solid line)
and simulated (dotted line) rail roughness (7.5m).

However, as expected, it can be seen that the smaller the experimental data collected, the lower the accuracy, but the results are a pretty good event for a short experiential extent. The results for the length of 7.5 are consistently below the relative error of 10% and always have the same order of magnitude of value result referring to each parameter analysed.

PSD is an essential parameter for identifying dominant spatial wavelengths present in a surface profile and understanding roughness behaviour at different length scales. It also plays a vital role in assessing noise sources related to the roughness of surfaces. In rail roughness analysis, PSD measures how different wavelength components contribute to the overall roughness. Short wavelengths may be associated with rolling noise, variations in the wear of rail surfaces or traces of material processing. In contrast, longer wavelengths are associated with airborne noise or vibration in precision machining or tribology applications.

Fig. 2.8.a compares the measured PSD and the PSD generated with the Weierstrass Mandelbrot function and provides information on how well the Weierstrass Mandelbrot model fits the actual roughness data for a length of 7.5 m. In this context, the simulated PSD is comparable in trend to the measured PSD. Furthermore, with the reduction of the roughness length up to 2.5 m, the results missed a wide range of wavelengths, but the coherence between the two PSD functions remains consistent across the 7.5 meters length, the alignment that also persists as the distance decreases as can be seen in Fig. 2.8.b.
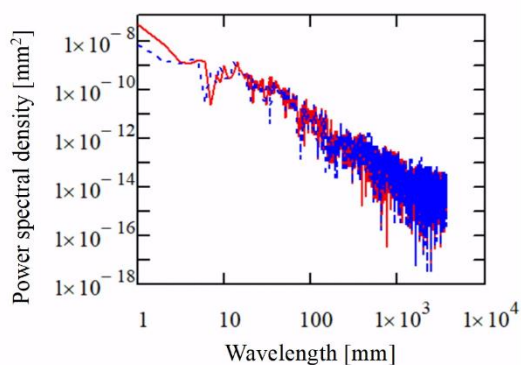

Fig. 2.8.a. Comparison between experimental (solid line) and simulated (dotted line) PSD function for roughness length 7.5 m.
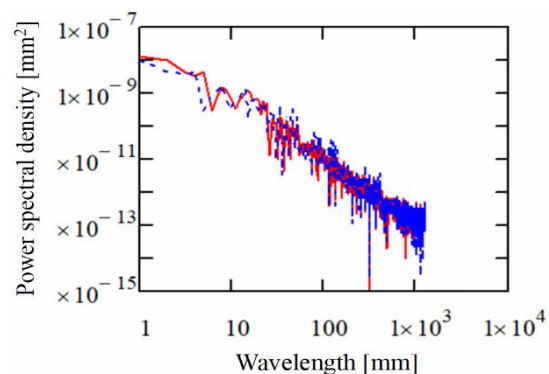
Fig. 2.8.b. Comparison between experimental (solid line) and simulated (dotted line) PSD function for roughness length 2.5 m.

An essential parameter in the railway system under examination is acoustic roughness, which records the height fluctuations of the running surface, correlating with the generation of rolling noise, and these variations are expressed as a function of the distance "x" along the running surface. Aligned with the guidelines of EN 15610:2019, in order to compare both measured and simulated roughness, the direct measurement approach was employed to characterise the roughness of the rail surface, precisely its correlation with the running noise referred to as "acoustic roughness." This characterisation is represented in the form of a one-third-octave band spectrum.

Fig. 2.5 shows that both measured and simulated rail acoustic roughness over a 7.5-meter length closely align, with a relative error of 7.31%. This alignment persists even when the measured length is reduced to 2.5 meters, with relative errors of 5.76% for 5 meters and 3.64% for 2.5 meters. Additionally, deviations from the TSI standards for measured and simulated roughness at 7.5 meters are 2.97 dB and 3.04 dB, respectively, indicating that shorter measurement lengths do not compromise the accuracy of the roughness data or the required wavelength range as per EN 15610: 2019 (2.8-250 mm).
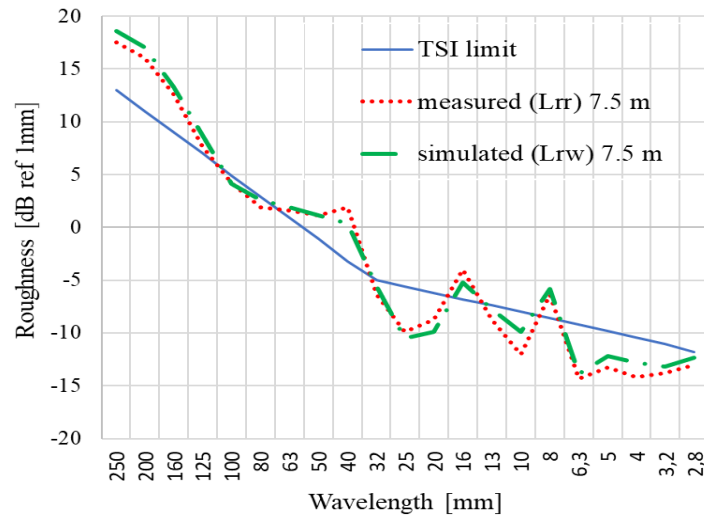
Fig. 2.9. Comparison between experimental (solid line) and simulated (dotted line) rail acoustic roughness determined for 7.5 rail roughness length.

Hence, Figs. 2.8-2.9 illustrate a notable alignment between graphs that show simulated and measured roughness, emphasising the WM model's robustness in capturing the surface roughness's nuanced characteristics.

Hereafter, the spacing parameters quantify the horizontal features of the surface irregularities and play a crucial role in roughness analysis, surface texture or a range of manufacturing processes, such as metal forming, where they are essential for maintaining uniform lubrication and performance during material shaping. While these parameters are significant in specific industrial applications, their importance is less pronounced in the railway field. Nonetheless, they assume an important role in the field of tribology, where their evaluation is paramount for optimising lubrication efficiency and surface interactions. The high number of points (HSC) is calculated by counting the number of high regions in a profile that exceeds either the midline or the level above the midline. The High Spot Count (HSC) shares similarities with the Peak Count (Pc), but the main difference between these two parameters is in the definition of the peak. For a peak to be counted in the Peak Count analysis, it must be succeeded by a valley that spans the entire bandwidth (upper and lower threshold). For the Peak Count, a threshold above and below the mean line is set at the same distance from the mean

line, and only peaks above this threshold are considered. The thresholds were set to $\pm\,0.05$ mm. The thresholds are intended to limit the number of peaks to "substantial peaks" to produce more stable parameters. Parameters like Peak Count and High Spot Count find their primary application in tribology, where they play a crucial role in manufacturing processes and quality control for coatings.

Based on the findings discussed earlier, it becomes evident that when considering a length of 7.5 meters, the spacing parameters extracted from the simulated roughness profiles demonstrate a remarkable closeness with the experimental roughness profiles. This proximity is exemplified by a relative error that remains notably below the threshold of 10%.

As expected, as the measurement distance is progressively reduced, a discernible reduction in the count of these spacing parameters is observed.

It is noteworthy, however, that certain parameters, specifically the High Point Count (HSC) and Peak Count, exhibit relatively higher errors when evaluated at shorter lengths.

These parameters are particularly suited for scrutinising the small metal material finishes and imperfections. Nonetheless, in the context of railway operations and the broader field of tribology, the emphasis often lies on broader-scale roughness attributes, and hence, these specific parameters might hold less relevance.

The hybrid parameters combine amplitude and spacing parameters and represent the last set of analysed parameters.

When considering a length of 7.5 meters, it becomes evident that the hybrid parameters extracted from the simulated roughness profiles, when compared to the experimental roughness profiles, consistently exhibit a convergence below a 10% relative error range. However, as the measurement distance is progressively reduced, a slight decrease in the count of these hybrid parameters becomes evident.

The anticipated trend of decreasing the number of parameters with the reduced measurement distance is a natural result, as fewer data points are collected for comparison with experimental results. Notwithstanding this minor reduction, the simulated results consistently uphold a level of accuracy and alignment, particularly given the relatively limited extent of its length. The robustness of the outcomes within the 7.5 meters distance preserves a comparable magnitude of values across the spectrum of analysed parameters and underscores the reliability of the method and its ability to provide valuable insights into the roughness characteristics under investigation.

For all parameters analysed, as the measurement length decreases, the resolution of the measuring instrument could become more critical. The measurement lengths of the experimental data can lead to challenges in capturing fine details and variations in the roughness profile, which can lead to fewer parameters obtained from simulated roughness in the relative error range of 10%.

The scale independence of the fractal method can be maintained in a certain range, but extreme length reductions can affect the accuracy of the measurements. While the fractal method provides a valuable way to model certain statistical properties of roughness, it may not fully capture all the intricate details and variations present on the surface at extremely small scales when reporting results to a scale of superior length. This could lead to identifying a smaller number of accepted roughness parameters.

Next, an in-depth analysis was conducted by juxtaposing all the roughness parameters extracted from the initial 7.5 meters experimental section with simulated roughness profiles spanning a range of 2.5 to 7.5 meters. The simulation intervals were systematically established at increments of 500 mm, thereby encompassing various length scales. Moreover, this comprehensive investigation extended to a comparison involving the simulated roughness at a minimum measured length of 1 meter, a requirement specified by the EN 15610 standard. In each instance of simulated roughnesses, the fractal parameters D and G_f were determined.

All parameters calculated for the measured roughness profiles as well as those obtained from the simulated roughness that falls within a margin of error of 10%, are presented in detail in Table 2.4. This thorough examination emphasises the effectiveness of the method in capturing and reproducing the characteristics of roughness while maintaining a high degree of fidelity to experimental data.

Table 2.1. Centralizer on the statistical parameters of experimental
and simulated roughness that falls within the relative error of 10% (7.5m).

Distance measured	7.5 m	7 m	6.5 m	6 m	5.5 m	5 m	4.5	4	3.5	3	2.5	1
No. Amplitude param.	16/16	16/16	15/16	14/16	13/16	13/16	13/16	13/16	12/16	12/16	12/16	11/16
No. Spacing param.	8/8	7/8	6/8	6/8	6/8	6/8	5/8	5/8	5/8	5/8	5/8	2/8
No. Hybrid param.	12/12	11/12	10/12	10/12	10/12	10/12	8/12	7/12	7/12	7/12	7/12	5/12
Total no. parameter	**36/36**	**34/36**	**31/36**	**30/36**	**29/36**	**29/36**	**26/36**	**25/36**	**24/36**	**24/36**	**24/36**	**18/36**

After careful examination of the data presented in Table 2.4, it can be seen that all simulated roughness parameters fall within an error of 10% for the measured roughness length of 7.5 m. This harmonious approximation extends convincingly up to a distance of 5 m, where many parameters still show notable agreement.

An analysis of data in Table 2.4 reveals that simulated roughness parameters are within a 10% error margin for lengths up to 7.5 m, extending to 5 m. However, a reduction in matching parameters

is noted as the measured length decreases to 2.5 m and 1 m, suggesting that 2.5 m is the optimal minimum for precise roughness analysis using the fractal method. Although some parameters deviate beyond the 10% error threshold, particularly those related to spatial characteristics, they hold less relevance in railway analysis. Despite a slight decrease in measurement precision for lengths shorter than 7.5 meters, this length is adequate to capture essential roughness characteristics as per the EN 15610 standard.

Regarding the analysis of the fractal parameters D and G_f, they are essential for the characterisation of the rail roughness and have unique values for a certain surface state.

Figs. 2.13 and 2.14 showcase the variation of fractal parameters D and G_f within each test subsection spanning 2.5 - 7.5 m of test section no. 1. Fig. 2.13 illustrates the relatively constant nature of the D fractal parameter, while Fig. 2.14 displays the diminishing trend of parameter G_f ($R^2 = 0.9986$) with increasing measured length. This suggests that fractal parameter D remains unaffected by sampling length and instrument resolution, whereas the parameter G_f shows dependence on sampling length, as existing literature suggests (*Zhang X., Xu Y. and Jackson R. L., 2017, Berry M. V. and Lewis Z. V., 1980*).

The agreement between the simulated roughness generated from rail measurements within TCF Romania further validates these dependencies.
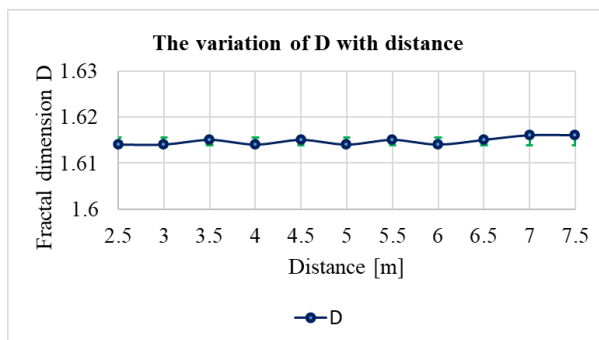

Fig. 2.13. Analysis of fractal
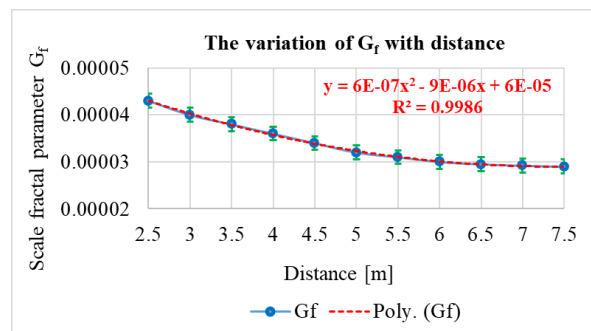dimension parameter D variation.

Fig. 2.14. Analysis of scaling
parameter G_f variation

In summary, the entire length of 950 m within the Făurei Testing Centre, Romania, from km area 6 + 900 to km area 7 + 850, showcases an average fractal parameter D value of 1.615 ± 0.00045 (95% confidence interval) with a coefficient of variation (CV) of 0.044% and parameter G_f holds a value of $3.379 \times 10^{-5} \pm 2.367 \times 10^{-6}$ (95% confidence interval) with a coefficient of variation CV = 8.754%.

Chapter 3

Fractal model of static friction behaviour in Hertzian roughness contact

3.1. Introduction

Contact mechanics, foundational in tribology, explores the analysis of stresses and deformations within the contact zone between bodies. Beginning with Hertz's pioneering work in 1882, which highlighted stress interactions between elastic solids, advanced methodologies have been developed to determine the real contact area in rough surfaces and to explore specific tribological phenomena such as wear, friction and dynamic contact.

This research aims to explore the static coefficient of friction within the context of Hertzian contact between rail and wheel, employing a methodology based on fractal approaches. The analysis is grounded in the Weierstrass-Mandelbrot model, which outlines the transition through four deformation states: elastic, the first two elastoplastic, and the fully plastic state. In this light, the static friction coefficient is considered to reflect an intrinsic property of the softer material in contact, with the surface microgeometry influenced by the fractal parameters D and G_f. Connecting these concepts, it should be noted that although the Hertzian contact surface is traditionally assumed to be homogeneous, this work enriches the perspective by considering fractal properties for the calculation of the actual contact area.

3.2. Static friction theoretical fractal model

Fractal characterisation of the equivalent roughness of the wheel and rail, is based on the Weierstrass Mandelbrot function (WM) (eq.2.5 chap. 2) and provides a more accurate description of how the surface roughness interacts at different scales during contact.

3.2.1. Analysis of contact with one asperity

The mechanical model of a single asperity is depicted through cosine waves, offering an understanding of surface roughness and contact mechanics at the microscopic level.

Based on the WM function, with a wavelength of $l=1/\gamma^n$, (l denotes a general wavelength or a characteristic scale applicable in a broad context, γ is a parameter that defines the frequency density in roughness analysis, and n is the integer number of items gathered by the series during the roughness measurement process), and it indicates the total number of data points considered in the analysis); the shape of individual asperity deformation is described as: (*Y. Yuan, 2016*):

$$y(x) = G_f^{(D-1)} l^{2-D} \cos \frac{\pi x}{l}, \quad -\frac{l}{2} \le x \le \frac{l}{2} \qquad (3.1)$$

where $y(x)$ represents the height of the roughness profile, D represents the fractal parameter, $(1 < D < 2)$, and G_f is the characteristic scaling length.

The deformation (δ) and amplitude (a_m) can be expressed in the following manner (Y. Yuan, 2016):

$$\delta = G_f^{(D-1)} l^{2-D} \left(1 - \cos \frac{\pi r^2}{2l} \right), \quad a_m = G_f^{(D-1)} l^{2-D}. \qquad (3.3)$$

Individual asperity deformation in contact with the rail surface can be elastic, elastoplastic, and plastic.

3.2.1.1. Elastic deformation regime

For the elastic regime in the context of Hertzian contact between wheel and rail, the focus is on the reversible deformation of asperities under load. In this regime, the materials return to their original shape once the load is removed. The elasticity of the materials is fundamental for absorbing and distributing the stresses without causing permanent changes.

Based on the Hertz theory (*Johnson K. L., 1987*), the critical deformation (δ_c) caused by an individual asperity, when in contact with a flat, rigid, smooth surface rail is:

$$\delta_c = G_f \left(\frac{2E}{k \cdot H_d} \right)^{\frac{2-D}{D-1}}, \qquad (3.4)$$

where, H_d is the hardness of the softer material, k represents the coefficient related to the Poisson ratio of the wheel (*Chang, W. R., Etsion, I., and Bogy, D. B, 1988*) with $k=0.454+0.41\nu$, and E is the equivalent Hertzian elastic modulus.

When the deformation δ equals the critical value δ_c, the individual asperity undergoes elastic deformation.

Subsequently, the dimensionless contact load in the elastic state (P_{se}) may be expressed by fractals depending on the roughness corresponding to the contact dimensionless area a_s as follows:

$$P_{se}(a_s) = \frac{4\sqrt{\pi} G_{fs}^{D-1}}{3} a_s^{(3-D)/2}, \quad P_{se} = \frac{P_e}{A_a E}, \qquad (3.10)$$

where, dimensionless P_{se} denote the contact loads of a distorted asperity in the elastic regime.

3.2.1.2. Elastoplastic deformation regime

In the context of Hertzian contact between wheel and rail, the elastoplastic regime is particularly significant as it determines how forces are transmitted and distributed across the contact asperities. The dimensionless contact loads in the first and second elastoplastic regimes (P_{sep1}, P_{sep2}) may be

expressed by fractals depending on the roughness corresponding to the contact dimensionless area a_s follows:

$$P_{sep1}(a_s) = \frac{2a_2}{3a_1} kk_{HE} G_{fs}^{2(D-1)(b_2-b_1)} \left(\frac{2}{kk_{HE}}\right)^{2(b_2-b_1)} a_s^{(1-D)(b_2-b_1)+1}, P_{sep1} = \frac{P_{ep1}}{A_a E},$$

(3.13)

$$P_{sep2}(a_s) = \frac{2a_{2p}}{3a_{1p}} kk_{HE} G_{fs}^{2(D-1)(b_2p-b_1p)} \left(\frac{2}{kk_{HE}}\right)^{2(b_2p-b_1p)} a_s^{(1-D)(b_2p-b_1p)+1}, P_{sep2} = \frac{P_{ep2}}{A_a E},$$

where P_{sep1} and P_{sep2}, denote the contact loads of a distorted asperity in the first and second elastoplastic regimes, and a_1, b_1, a_2, b_2, a_{1p}, b_{1p}, a_{2p} and b_{2p} are the constant (*Kogut L. and Etsion I. 2002*)

3.2.1.3. Plastic deformation regime

Regarding the plastic regime, the focus is on the asperities' irreversible deformation when the applied load surpasses the material's yield point. In this state, the asperities are permanently altered and do not return to their original shape post-load, affecting the contact surfaces.

The full plastic regime of a deformed asperity falls within the range $\delta_s \geq \delta_{cs}$. The dimensionless contact load in the plastic regime ($P_{sp}(a_s)$) could be written as follows:

$$P_{sp}(a_s) = k_{HE} a_s, P_{sp} = \frac{P_p}{A_a E},$$

(3.14)

where P_p, with dimensionless form, P_{sp}, denote the contact loads of a distorted asperity in the plastic regime.

Finally, the dimensionless total contact load (P_{st}) is given by:

$$P_{st}(D, G_{fs}, a_s) = P_{se}(D, G_{fs}, a_s) + P_{sep1}(D, G_{fs}, a_s) + P_{sep2}(D, G_{fs}, a_s) + P_{sp}(D, G_{fs}, a_s)$$

(3.15)

when $\delta_s \geq \delta_{cs}$, it follows that $a_s > a_{cs}$.

Correspondingly, within the context of the present model, the total normal load denoted as F_n also emerges as the accumulation of the contact loads linked to the four regimes. Normal total load and its dimensionless forms could be elaborated upon as follows:

$$F_n = F_e + F_{ep1} + F_{ep2} + F_p$$

(3.21)

The equation gives the dimensionless total normal contact load for real contact area:

$$F_{nst}(a_{ls}) = F_{es}(a_{ls}) + F_{ep1s}(a_{ls}) + F_{ep2s}(a_{ls}) + F_{ps}(a_{ls})$$

(3.24)

This formulation captures the comprehensive impact of various contact regimes on the cumulative normal load, offering a refined understanding of the contact behaviour between simulated surfaces with fractal roughness.

3.2.2.   Tangential contact load and static friction coefficient

In the case of the friction analysis described above, the tangential load is the force that tries to initiate sliding or relative motion between wheel-rail contacting surfaces. Only the contacting asperities (microscopic surface irregularities) that undergo the fully elastic and the first elastoplastic regimes are able to support the tangential load (*Kogut L. and Etsion I., 2003; Kogut L. and Etsion I., 2004; You Y., 2010, (Zhang C. et al., 2022, You J. M., 2010; Zhao B., Xu H., & Lu X., 2019)*). This means that only certain portions of the contacting surfaces, where the deformation remains within specific limits, can resist the force attempting to cause sliding. Furthermore, at the stage of sliding inception, the final yielding or plastic deformation occurs at the edge of the contact spot. This assumption is based on the distribution of the principal stresses within a deformed asperity at the interface (*Zhang C. et al., 2022, You J. M., 2010; Zhao B., Xu H., & Lu X., 2019*). This indicates that under the influence of the tangential load, the material experiences plastic flow, losing its ability to withstand further tangential loads without undergoing significant deformation.

The Tresca criterion determines the onset of plastic deformation by asserting that yielding starts when the material's maximum shear stress reaches a specific threshold (*K. L. Johnson*). Utilising this criterion, the maximum dimensionless tangential load, T_{ts} *(a_{ls})*, can be deduced for surfaces with fractal roughness.

$$T_{ts}(a_{ls}) = \frac{8k_{yE}}{\pi(6-3\upsilon)}\left(A_{es}(a_{ls}) + A_{ep1s}(a_{ls})\right) + \frac{8(2v-1)}{\pi(6-3v)}\left(F_{es}(a_{ls}) + F_{ep1s}(a_{ls})\right),$$

$$k_{yE} = \frac{\sigma_y}{E}$$

(3.25)

where k_{yE} represents the yield ratio and σ_y, yield stress.

Then, the static friction coefficient $\mu_s(a_{ls})$ in the can be expressed as:

$$\mu_s(a_{ls}) = \frac{T_{tf}(a_{ls})}{F_{ns}(a_{ls})}$$

(3.26)

3.3.   Experimental measurement

The flat specimen was made of unhardened and unalloyed steel, type R260 (EN 13674-1:2018) with a Brinell hardness of 285 HBW, and the cylinder specimen was made of surface-treated steel, type ER7 (EN 13262:2021), with a Brinell hardness of 265 HBW. These wear-resistant materials are used for the rails and wheels in railway systems.

Rail roughness, measured at the Faurei Test Centre (see Chapter 2), was assessed using the m|rail trolley equipment. In the same way, wheel roughness from the Lema locomotive class 048 was evaluated using the m|wheel system.

3.4. *Methodology*

In the framework of this study, we aimed to determine the static friction coefficient by employing a fractal approach, which combines the fundamental principles of fractal geometry with the mechanics of contact in both Hertzian wheel-rail systems and cylinder-plane specimen interactions involving rough surfaces.

Within the scope of this study, the μ_s were determined by employing a fractal approach, which combines the fundamental principles of fractal geometry with the mechanics of contact in Hertzian wheel-rail systems and cylinder-plane specimen interactions involving rough surfaces. From this perspective, the static friction coefficient is perceived as an "intrinsic property" of the softer material of the two in contact within the context of a specific surface micro geometry, defined by the unique fractal parameters D and G_{fs}.

Fractal geometry provides an efficient method for characterising contact surfaces. This approach is relevant for both the cylinder-plane contact samples in the laboratory and the wheel-rail contact.

The structure-function (SF) method, following the methodology presented in Chapter 2, was applied to estimate these parameters, as detailed in equations 2.1 to 2.4. Subsequently, the equivalent fractal parameters were calculated to simplify the contact analysis between the two rough surfaces, whether the reference is to the cylinder-plane samples or the wheel-rail. The *SF* of the surface with equivalent roughness was determined using the following relation:

$$SF(\tau) = SF_r(\tau) + SF_w(\tau) \qquad\qquad (3.27).$$

Then, the WM function outlined in eq. (2.5) from Chapter 2 was used, and their simulated equivalent roughness was derived, yielding fractal parameters. From these analyses, distinct sets of fractal parameters have resulted.

For the analysis of Hertzian contact parameters, three scenarios were investigated for cylinder-plane specimens with roughness, each associated with a specific normal force of 20 N, 40 N, and 60 N. Within the study of Hertzian wheel-rail contact, focus was directed to a specific case where a normal force of 103.00 kN was applied to wheel number one.

The nominal areas (A_{a1}- A_{a4}) for the cylinder-plane material pairs, as well as the wheel-rail pairs, were determined based on the Hertzian contact semi-axes of the wheel and the cylinder, the applied external forces, and the material properties of the specimens (Esveld C,2001, Thompson D. J., 2009; Otero Yugat J., 2009).

The analysis encompassed four deformation regimes: elastic, first elastoplastic, second elastoplastic, and fully plastic, culminating in the determination of the static friction coefficient for these four scenarios.

3.5. *Results and discussions*

All deformation regimes were analysed to determine the static friction coefficient and contact parameters considering different values of the dimensionless scale parameter G_{fs} and the fractal parameter D.

3.5.1. *Elastic deformation regime*

3.5.1.1. Critical area

In this section, the first presentation covers the variation of the dimensionless critical area (a_{cs}) in relation to the fractal parameter D and the dimensionless critical deformation (δ_{cs}), as illustrated in Figures 3.3. (a, b). The determination of a_{cs} is conducted in accordance with Equation 3.7, and δ_{cs} is calculated following Equation 3.11.
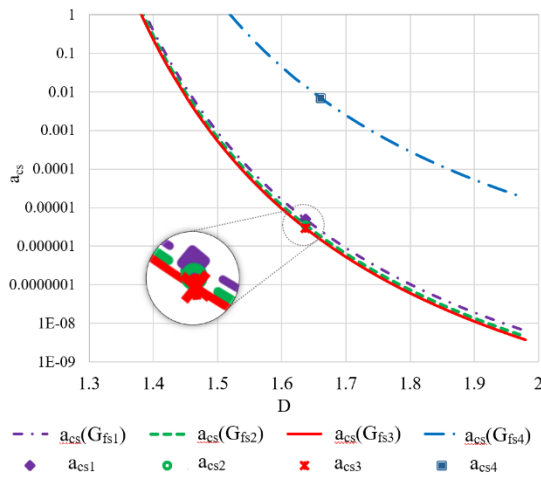
Fig. 3.3. (a) Variation critical area acs with variable Gfs and D fractal parameters
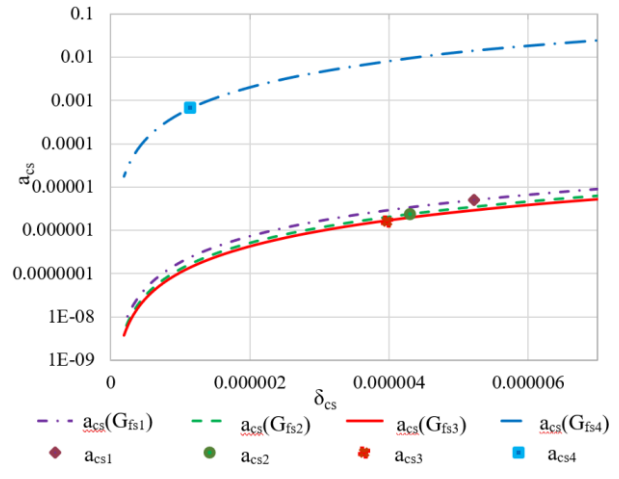
Fig. 3.3. (b) Variation critical area a_{cs} with deformation δcs with variable G_{fs} and D is constant
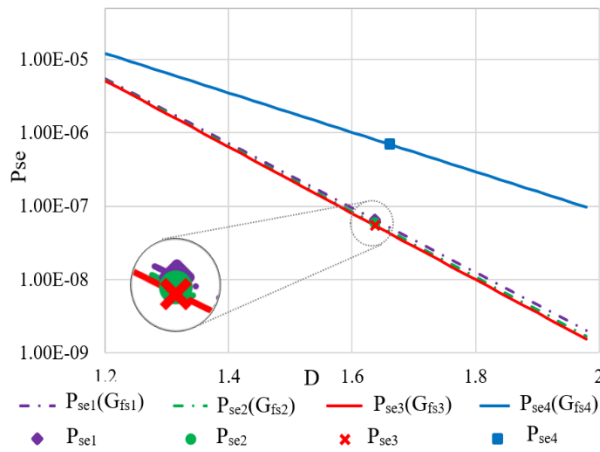
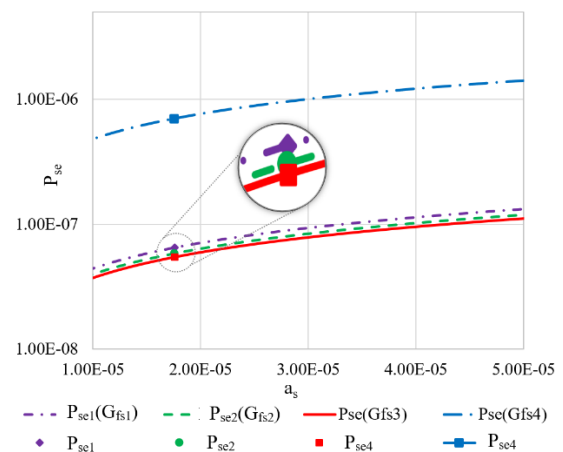Fig. 3.4. (a) Variation contact load P_{se} with D variable.

Fig. 3.4. (b) Variation contact load P_{se} with spot area a_s variable.

In Figure 3.4(a), an enhanced dimensionless elastic contact force (P_{se}) is associated with smaller fractal dimensions (D), which denote smoother surfaces, and when paired with larger scale parameters (G_{fs}), an expansion of the contact area within the elastic regime is witnessed, leading to an improved contact load.

Observations of Figure 3.4(b) confirm that the dimensionless elastic contact force (P_{se}) increases with the enlargement of the contact spot area (a_s). This phenomenon is also evident in the wheel-rail contact. However, in the case of cylinder-plane specimens, a decrease in P_{se} with an increase in the normal force indicates a concentration of pressure in a smaller contact area and a more intense interaction at the microscopic level.

3.5.1.2. Elastoplastic deformation regime

The irreversible changes in material behaviour under load can identify the transition into the elastoplastic regime.

Following this, the contact load variations in the elastoplastic regime, denoted as P_{sep1} and P_{sep2}, are showcased in relation to the fractal parameter D and spot area as presented in subsequent figures 3.7. (a, b) and Equation 3.13.
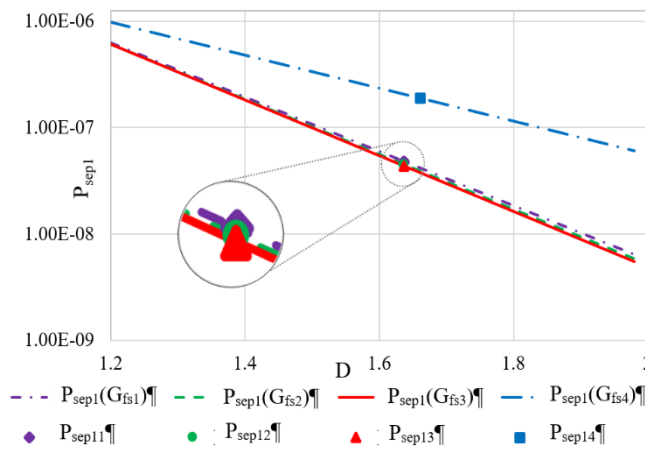

Fig. 3.7. (a) Variation contact load P_{sep1} with variable D and G_{fs} fractal parameters.
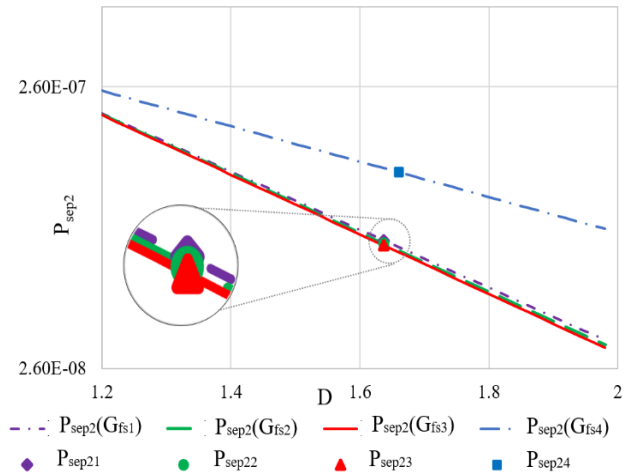
Fig. 3.7. (b) Variation contact load P_{sep2} with variable D and G_{fs} fractal parameters.

A higher fractal parameter D in this range signifies a rougher surface topology. With more irregular surfaces, there are more asperities. However, not all asperities will make adequate contact. The more pronounced roughness (higher D) means the asperities that do come into contact might be those that are taller or more prominent, leading to smaller Psep1, as they carry the bulk of the load and potentially undergo greater local deformations (Figure 3.7. (a)).

Regarding the similarity of P_{sep1} with P_{sep2} (Figure 3.7. (b) and elaborated through Equations 3.8 and 3.13), while the foundational principles remain the same, the interaction forces and

deformations are more pronounced due to more in-depth elastoplastic behaviour. A decrease in D in this regime results in a rise in P_{sep2} compared to P_{sep1}.
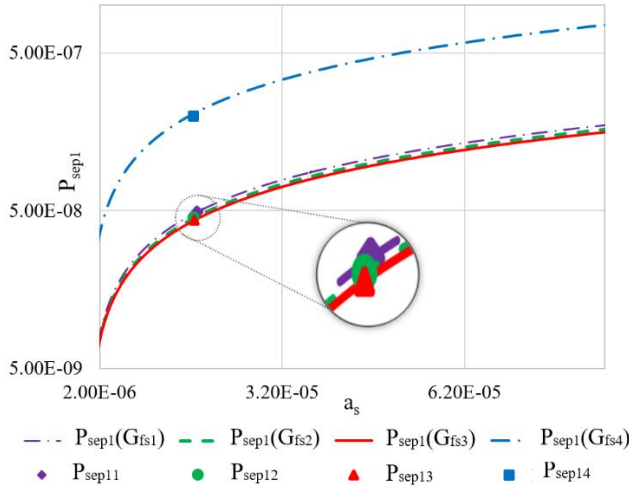

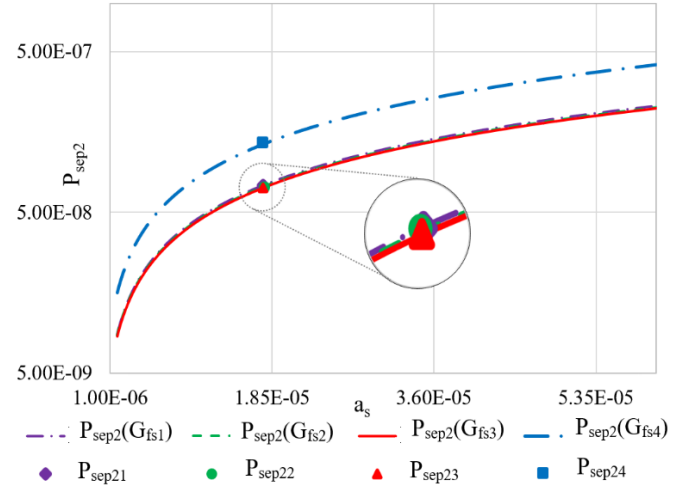Fig. 3.8. (a) Variation contact load P_{sep1} with variable D and spot area a_s.

Fig. 3.8. (a) Variation contact load P_{sep2} with variable D and spot area a_s.

Figures 3.8. (a, b) depict the first and second elastoplastic regimes. There is a diminished contact area for a higher D value and G_{fs} constant (a_s). Conversely, this contact load decreases as D decreases, following the same trend as Figure 3.4. (b). This trend illustrates the profound influence of fractal dimension D on contact mechanics within these two elastoplastic regimes.

3.5.1.3. Plastic deformation regime

Figure 3.9 highlights the relationship between the contact load P_{sp} (Equation 3.14) in the plastic regime and the fractal parameter D and the spot area a_s. In these figures, it is observed that the whole plastic deformation regime remains unaffected by the parameters D and G_{fs}.
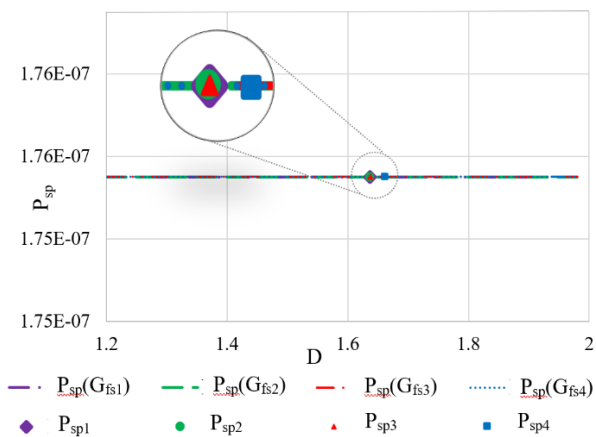

Fig. 3.9. (a) Variation contact load P_{sp} with fractal parameters D.
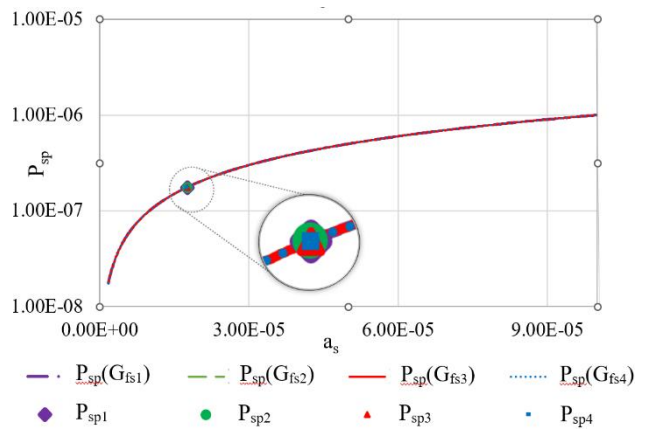
Fig. 3.9. (b) Variation contact load P_{sp} with spot area a_s

At this stage, asperities undergo significant deformations, and subsequent interactions are more related to the plastic behaviour of the material than to its initial state or its fractal properties.
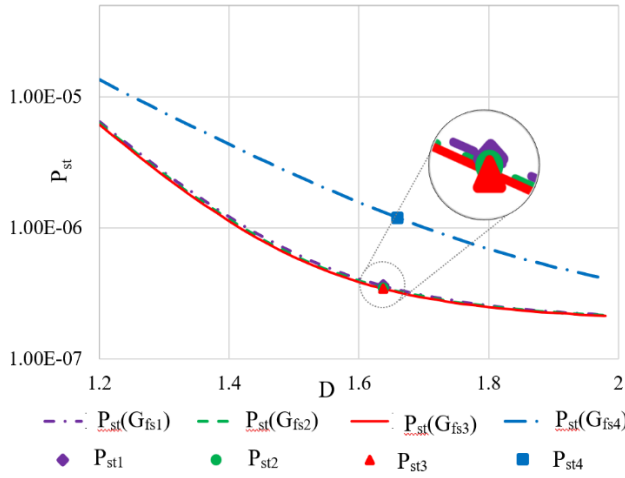

Fig. 3.10. (a) Variation contact load P_{st} with variable D and G_{fs} fractal parameters.
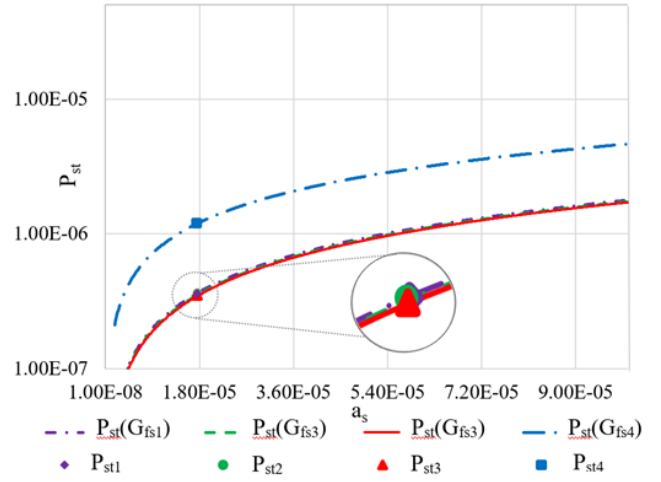
Fig. 3.10. (b) Variation contact load P_{st} with variable as, a_s and G_{fs} fractal parameters.

Figure 3.10. (a, b) depicts the total contact load, P_{st}, (eq. 3.15) and its interplay with the fractal parameters D and G_{fs}. Mirroring the trends observed for P_{se}, P_{se1}, and P_{se2}, a_s, D and G_{fs} vary, P_{st} also demonstrates a similar response.

3.5.2. Total normal load

Figure 3.12 shows the fluctuation of the dimensionless total normal load (F_{nst}) in relation to the fractal parameter D and the largest spot area a_{ls} which can span between 0 and 1. This correlation is quantified by Equation 3.24, which provides a mathematical foundation for understanding the observed trends.
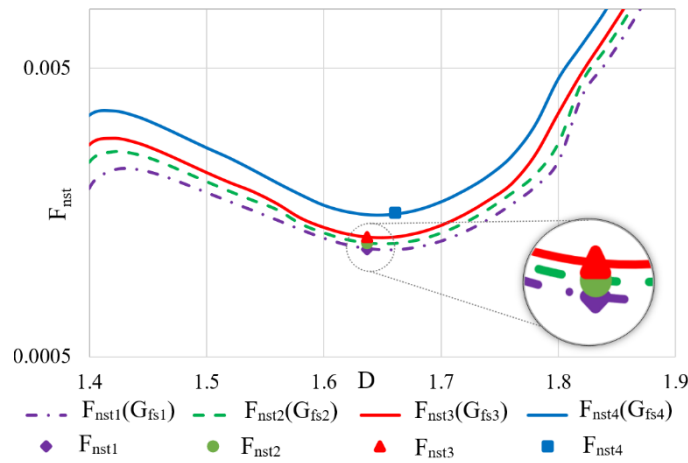

Fig. 3.12. Variation contact load F_{nst} with variable fractal parameter D and maximum spot area a_{ls}.

Figure 3.12. details the relationship between the total normal load, F_{nst}, and the parameters D, G_{fs} and a_{ls}. Thus, it is observed that the total force, F_{nst}, increases with the expansion of the area of the predominant spot. The effect of D on F_{nst} is evident only within the range D from 1.35 to 1.9. F_{nst} appears to be independent outside this range, suggesting that D is not the primary factor governing F_{nst}.

Such behaviour suggests that other mechanisms or properties at the material level or surface interactions might dominate under these conditions.

3.5.3. *Static friction coefficient*

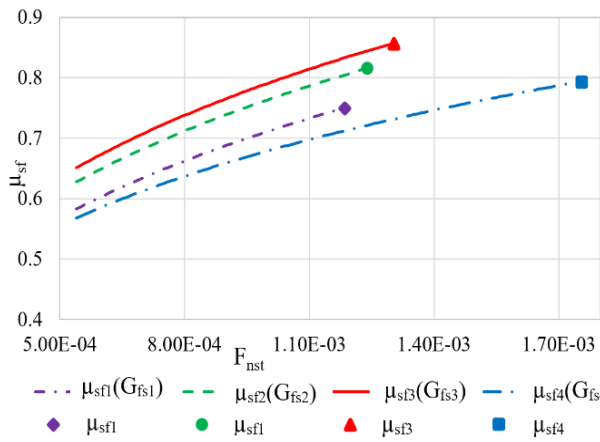Figures 3.13. (a, b) depict the dependency of COF on F_{nst} (Eq. 3.26) and the fractal parameter D.

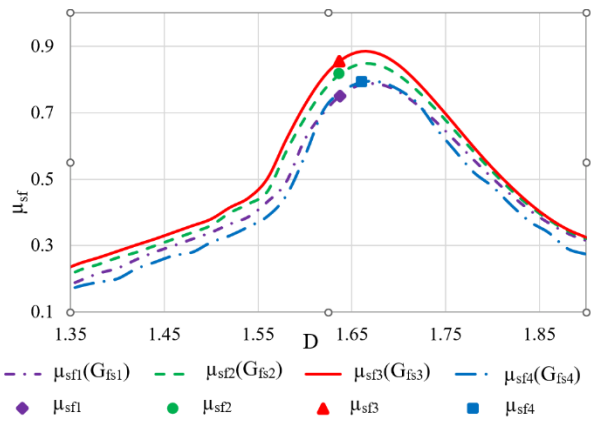Fig 3.13. (a) Variation contact load F_{nst} with static friction coefficient (μ_{sf}).

Fig 3.13. (b) Variation static friction coefficient (μ_{sf}) with variable fractal parameter D.

In the graph 3.13. (a), for cylinder-plane pairs (μ_{sf1}, μ_{sf2}, and μ_{sf3}), the static coefficient of friction (COF) increases with the dimensionless total normal load. This trend aligns with expectations since a greater normal force enhances the interlocking of surface asperities, thereby increasing friction.

Conversely, for the wheel-rail pair (μ_{sf4}), a lower static COF is observed even under significantly higher F_{nst}. This phenomenon may be attributed to the presence of a lubricating film or lubricated conditions in the wheel-rail contact zone, which can reduce friction. Additionally, at very high normal forces, such as those in wheel-rail contact, asperities might be flattened or deformed more extensively, potentially leading to an apparently larger contact area but with less effective micro-level interlocking, resulting in a lower static COF. Nonetheless, the increasing trend suggests that even under these conditions, as the normal force continues to rise, the interactions between asperities and resistance to sliding begin to have a greater impact, leading to a gradual increase in the COF.

From the example shown in Figure 3.13. (b), it is observable that at low G_{fs} values, the static coefficient of friction (COF) reaches its maximum and declines with an increase in Gfs, highlighting

the significant influence of the scale factor on friction characteristics. Conversely, the static COF can be detected by D only within the range of 1.3-1.9. Outside this range, the absence of a discernible static COF could be due to specific surface interactions, deformation characteristics, or insufficient roughness engagement to produce measurable friction.

The COF is at its maximum for D in the range of 1.6-1.7 because this fractal dimension range corresponds to the most optimal balance between surface adherence and the elastic deformation capacity of the asperities. At these values, the asperities are sufficiently engaged to create resistance to sliding but are not so deformed that they allow easier sliding. A D of approximately 1.6-1.7 may reflect a density and distribution of asperities that maximise the interaction and interlock between the contacting surfaces, thus leading to an increased COF.

For the wheel-rail pair, the COF value is the lowest shown in the graph, which can be explained by several factors specific to railway systems. Firstly, the wheel-rail interface is often subject to lubrication conditions, either from natural environmental lubrication or the deliberate application of lubricants to reduce wear and facilitate smooth motion.

Chapter 4

Stick-Slip Phenomena and Acoustic Emission in the Hertzian Linear Contact

4.1. Introduction

This study focused on using Acoustic Emission (AE) signal parameters requiring minimal hardware and software resources. These parameters can be derived from a signal captured by a versatile data acquisition system used for mechanical tests. The objective was to detect the occurrence of the stick-slip phenomenon in dry friction conditions at Hertzian linear contact points using these low-demand AE signal parameters.

The study broadens its research scope by incorporating the validation of the experimentally determined static friction coefficient by comparing it with the value obtained from fractal analysis, both measurements being conducted under stabilised regime conditions. This approach aims to reinforce understanding of the friction phenomenon and verify the accuracy of the methods used in calculating the static friction coefficient. By directly linking these research aspects, the aim is to detect the stick-slip phenomenon through acoustic emission parameters and to conduct a deeper analysis of the relationship between friction behaviour and low driving speeds, a central point in the study of tribology principles.

4.2. Experimental Model-Geometry and Material of Specimens

The experimental setup presented in this paper was carried out in CERT UMT-2 Tribometer, which is used to test the stick-slip phenomenon of different materials. Fig. 4.2 shows the test system with the upper and lower specimens connected to the tribometer. To perform these experimental tests, the tribometer was adapted to the specific slip conditions for Hertzian linear contact.

The adhesion at the molecular level and the elastic–plastic deformations at the roughness level are both responsible for friction, which in turn is responsible for tangential force (*Eid H., 2011, Mulakaluri N., 2011, Persson B. N. J., 2000*). A CETR AE-5 AE sensor with a frequency range between 0.2 MHz and 5 MHz, integrated with the UMT-2 tribometer, was intended to measure the acoustic emission signals during the friction test. The AE signal and those related to force and position, was acquired by the CETR UMT control unit at a 200 kHz sampling rate. The AE signal was amplified with a gain of 60 dB, and its r_{rms} value was calculated every 0.5 s.
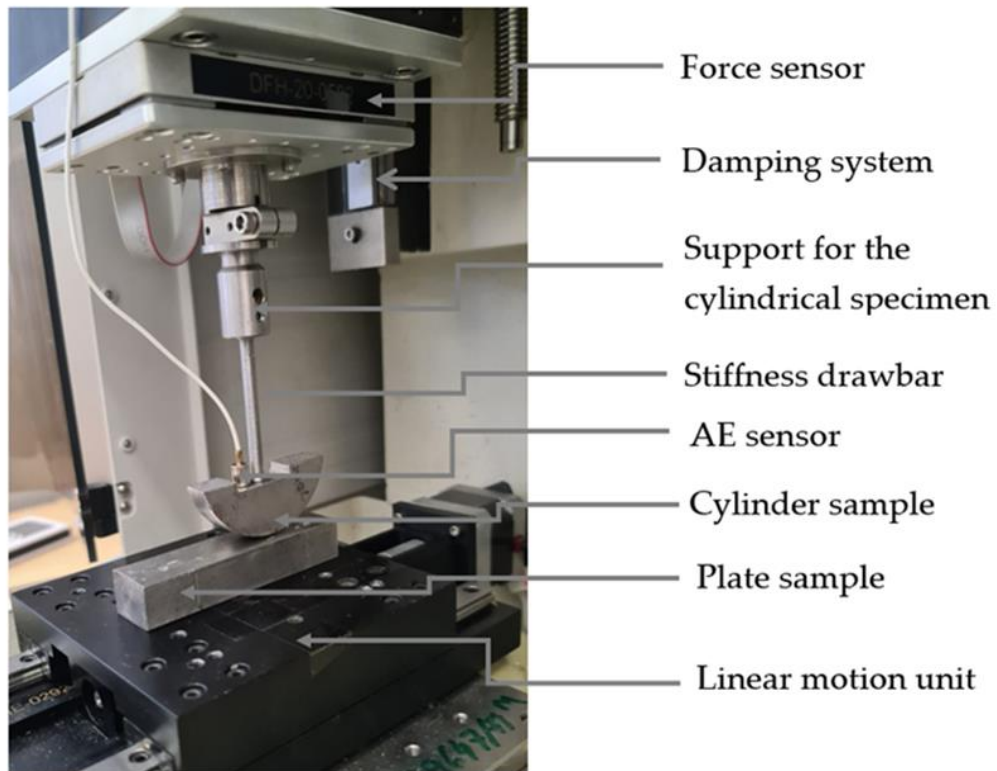
Fig. 4.2. Tribometer to study the phenomenon of stick-slip.

The primary purpose of the experimental tests was to determine the evolution of the static and kinetic friction coefficients of the stick-slip phenomenon accompanied by the appearance of the acoustic emission at the Hertzian linear contact.

4.3. *Methodology*

One goal of this study was to demonstrate that the basic parameters of the AE are suitable and sufficient to detect the SS phenomenon and, thus, the adapted configuration of the Tribometer UMT-2 prepared for this type of experiment led to a simplified but sufficient analysis of the AE signals, avoiding the requirements of standard AE equipment. Moreover, the fundamental objective of the experimental tests carried out was to analyse the correlations of the AE and COF parameters, depending on the low and very low driving speeds, because the initiation of the relative motion between two bodies under friction is a fundamental and essential problem in understanding the friction principle in tribology.

Friction force, normal force, and AE were directly measured by transducers. Indirectly, averages of each COF type (static, kinetic, amplitude), sliding speed, energy consumed by friction, and several AE parameters (counts, amplitude, energy) were calculated.

The analysis involved 12 tests to study stick-slip phenomena, determining static and kinetic friction coefficients and stick-slip amplitude for each jump sequence.

The energy generated by the acoustic emission (W_{AESt} and W_{AESl}) during the stick-slip period is defined as the integral (area) of the square voltage (V_{AE}) emitted over time.

The instantaneous speed in the slip phase is defined as the derivative of the distance the cylindrical specimen covers during the slip time.

The analytical approach taken in this study delves into the slip oscillations observed in the stick-slip phenomenon, considering the kinetic friction coefficient as a function of driving speed and the static friction coefficient as a function of stick time. Referencing pivotal research such as that by (*F. Heslot 1994, Baumberger T. 1996, Caroli C. and Noziers P. 1995, and Baumberger et al. 1995*), the studies highlight a clear logarithmic relationship between the static friction coefficient and the stick time (t_{stick}), of the form $\mu_s(t) = a_s + b_s \ln\left(\dfrac{t}{t_0}\right)$ where t_0 represents an arbitrary normalisation constant.

This indicates that μ_s is contingent on the interaction history and the prior conditions experienced by the surfaces, suggesting that the static friction coefficient is not just an instantaneous property but also a reflection of the material's "memory" or the cumulative history of contact and deformation.

By analysing the dependence of the static friction coefficient on the stick time and the static and kinetic friction coefficients as a function of the driving speed, logarithmic approximations were applied to the resulting data, which allowed the determination of the memory length (L_{mc}) (T. Baumberger, 1995) for the three applied contact forces and, consequently, the static coefficients at the targeted speed of 10^{-4} mm/s.

This study calculated an average stick time for each speed and load type from experimental data, providing a general overview of adhesion durations under various operating and loading conditions in tribology and contact mechanics. The concept of L_{mc} (memory length) was introduced, representing the distance over which past interactions of a surface influence its current behaviour, essentially acting as the surface's 'memory' of past tribological events. The creep time, a crucial factor in the stick-slip phenomenon for Hertzian contacts (cylinder-plane or wheel-rail), was also determined. The experimentally obtained static friction coefficients in a stabilised regime at a speed of 10^{-4} mm/s were compared and validated with those determined by the fractal method, as detailed in Chapter 3.

4.4.   Results and Discussions

The friction coefficient evolution accompanied by AE is presented as an example of the results obtained for the driving speed of 0.01 mm/s at normal forces of 20-60 N. (Fig.4.3.a-c) and the friction coefficient evolution for the force of 60 N at the four driving speeds (Fig.4.3.d). In all cases, the presence of the stick-slip phenomenon was confirmed by COF variation.

In general terms, the stick-slip jumps coincided with the sudden increases in AE, although for a 20 N load, this coincidence was not always present.
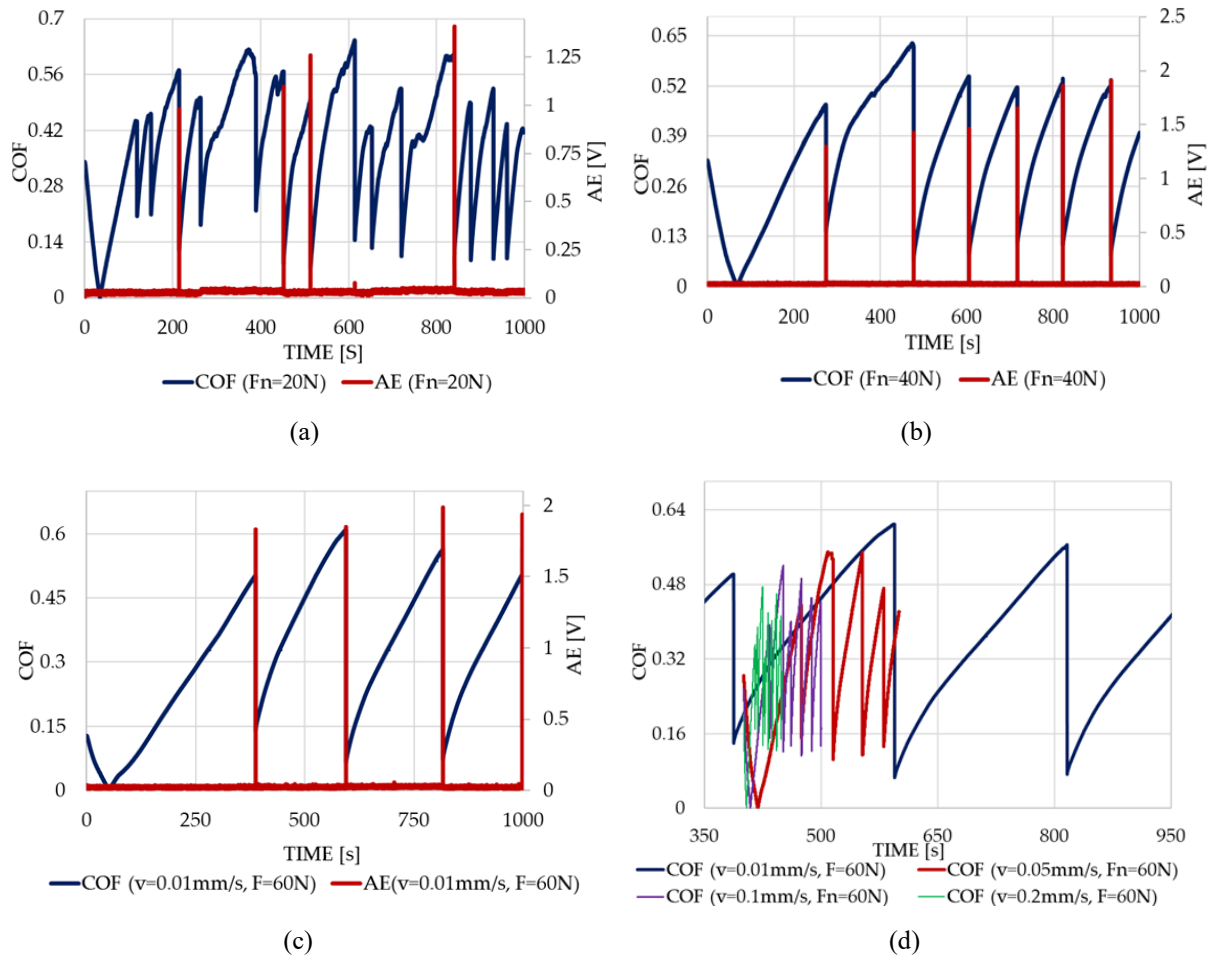

Fig. 4.3. COF and AE amplitude with a driving speed of 0.01 mm/s
for the normal force of 20 N (a), 40 N (b), and 60 N (c).
Comparison of COF results over time at 60 N force and all driving speeds (d).

Fig. 4.3 shows the static and kinetic friction coefficients and the stick-slip amplitude for different driving speeds. As expected, the static and kinetic friction coefficients decreased as the driving speed increased to a specific stiffness. Both friction coefficients increased with the soldering time due to the phenomenon of "saturation" of the real contact area, so the higher the driving speed, the shorter the soldering time and the lower the static and kinetic coefficients (*Ozaki S., 2020, Lontin K., 2021*). The increase in driving speed also reduced the contact surface and accordingly, the friction coefficient tended to decrease, giving, as a result, a stick-slip movement of lower amplitude (measured by the difference between the static and kinetic COFs), as can be seen in Fig.4.5c, and higher frequency, as shown in Fig.4.5d.
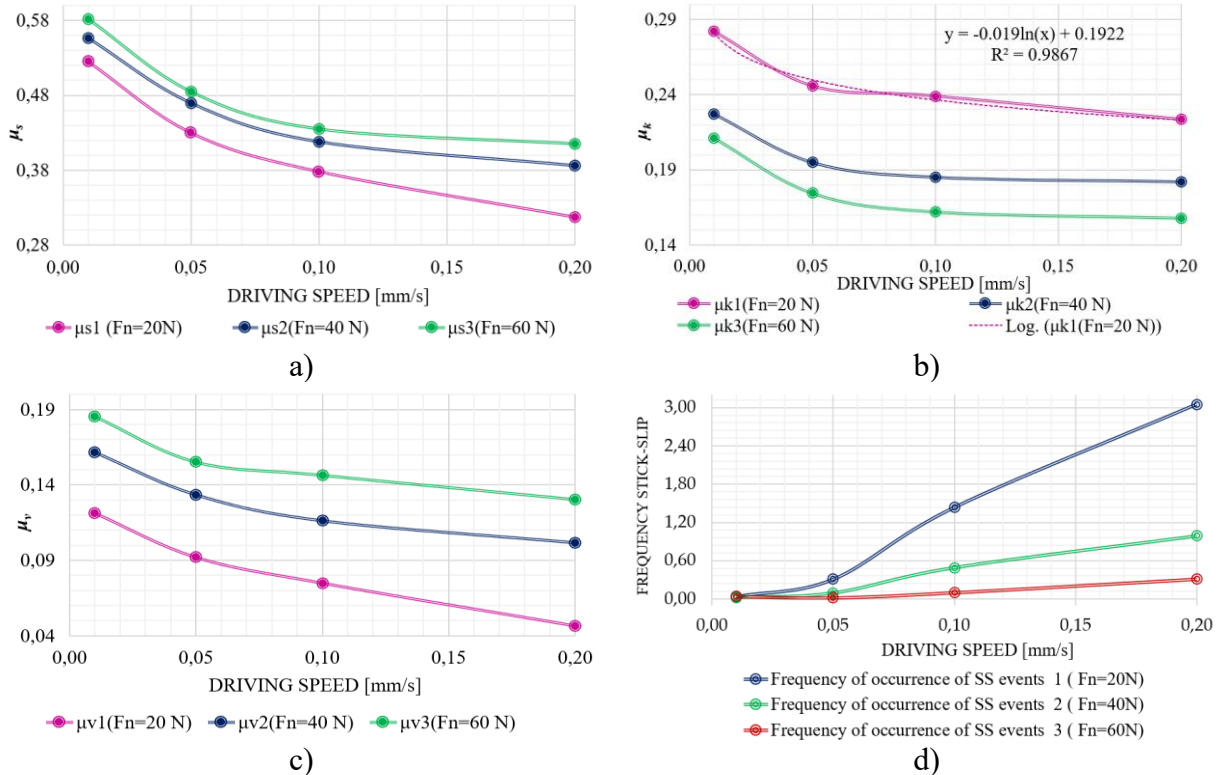
Fig. 4.5. The influence of the driving speed and normal force on the friction coefficients:

a) static friction coefficient, b) kinetic friction coefficient, including the fitted curve of the kinetic friction

coefficient with a force of 20 N, c) the amplitude of the stick-slip phenomenon,

d) with the frequency of the number of the stick-slip jumps.

In addition, Fig.4.5b shows the dependence between the kinetic friction coefficients on the driving speed, which decreases with increases in the driving speed of the surface, approximated by the logarithmic curves of the form $y = a + (b \ln (x))$ as has been previously found by Helstot and Caroli (*Heslot F., 1994, Caroli C., 1995)*.

Regarding the acoustic emission, as a general trend, there was the continuous activity of low AE in the stick phase; however, there was a burst emission of high amplitude in the sliding phase, and both were dependent on the normal load.

It is easy to see that the AE peaks appeared only at the jumps from the stick to the slip (the transition from static friction to kinetic friction), although they took place with a delay of a few milliseconds compared to the COF. This delay of the AE could be explained by the finite propagation speed of the AE elastic waves compared to the moment of the initiation of the slip phase (Fig.4.6).

In both the stick and slip phases, the counts of AE increased with the driving speed and decreases in the normal load. In fact, the higher the frequency of the stick-slip movement, the higher the AE counts. For each slip phase sequence in a test, each AE count was calculated over the slip time and, finally, mediated for each test. Likewise, for the stick phase, the AE counts were determined for each sequence over the stick time, and finally, an average was determined for each test. Therefore, a

low frequency, higher amplitude slip-stick movement gives a relatively low count of AE with the burst aspect, mainly occurring at the beginning of the slip movement.
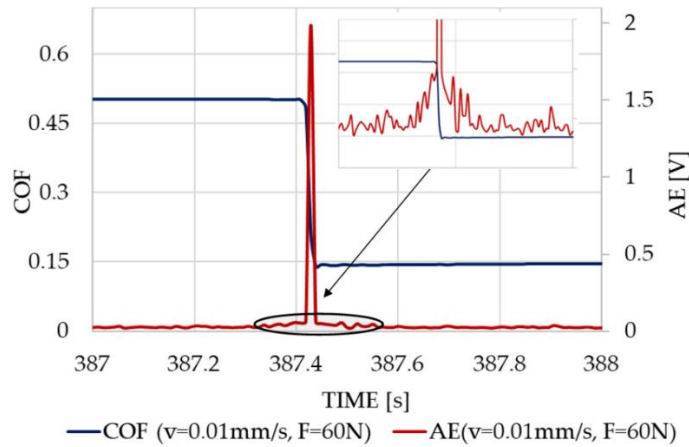

Fig. 4.6. The friction coefficient variation and acoustic emission variation (peak extracted).

The amplitudes of the AE signal were plotted against driving speed for different loads (Fig. 4.9). In general terms, the AE amplitudes for both the stick and slip phenomena seem to be rather related to the kind of stick-slip movement: the increase in the normal force and the decrease in driving speed led to an increase in the stick-slip movement amplitude, with a consequent rise in the amplitude of the AE bursts. In addition, the amplitude in the stick phase was significantly lower than the amplitude in the sliding phase (Fig. 4. 9. a, b), as was expected, since the AE caused during the stick phase was only prompted by the contact surface deformation, while for the slip phase, other phenomena, such as a part of the plastic deformation occurred. In the process of transmitting normal forces between the two bodies and in the presence of relative motion, the "third body" was formed with properties specific to the material couple. Thus, the structure of the material changed, the existing microcracks joined, and new cracks appeared, especially during the appearance of plastic deformations (Fig. 4.5). It was also observed that the AE amplitude follows a logarithmic curve, similar to the friction coefficients, depending on the movement speed.
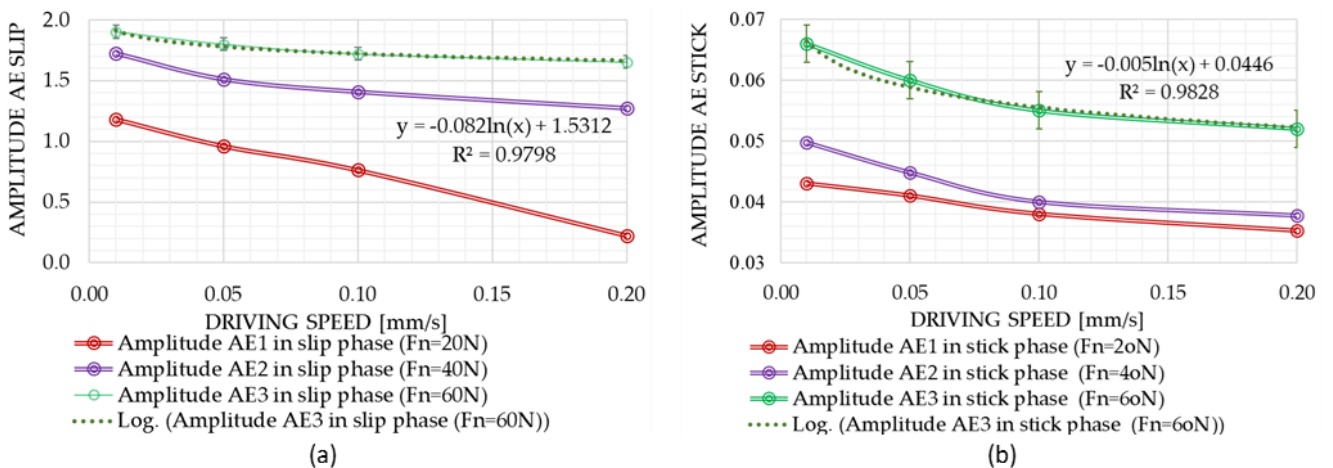

Fig. 4.9. Variation in AE amplitude with driving speed in slip phase (a) and stick phase (b).

Knowing that the amplitude of AE is correlated to the amplitude of the stick-slip movement, and the number of counts seems to be rather independent of the amplitude of the movement, it seems that the energy consumed by friction (W_{COF}) and the AE (W_{AE}) energy could also be related. The energy consumed by friction (W_{COF}) and the AE (W_{AE}) energy were calculated for the three forces, 20, 40, and 60 N, and for each phase of soldering and sliding (Fig. 4.10). In general terms, the higher the amplitude of the stick-slip movement, the higher the energy consumed by friction (W_{COF}) due to increases in the friction force and sliding distance, and the higher energy generated by AE, due to the intensity of the deformation mechanisms in the contact zone.

(a)

(b)

(c)

(d)
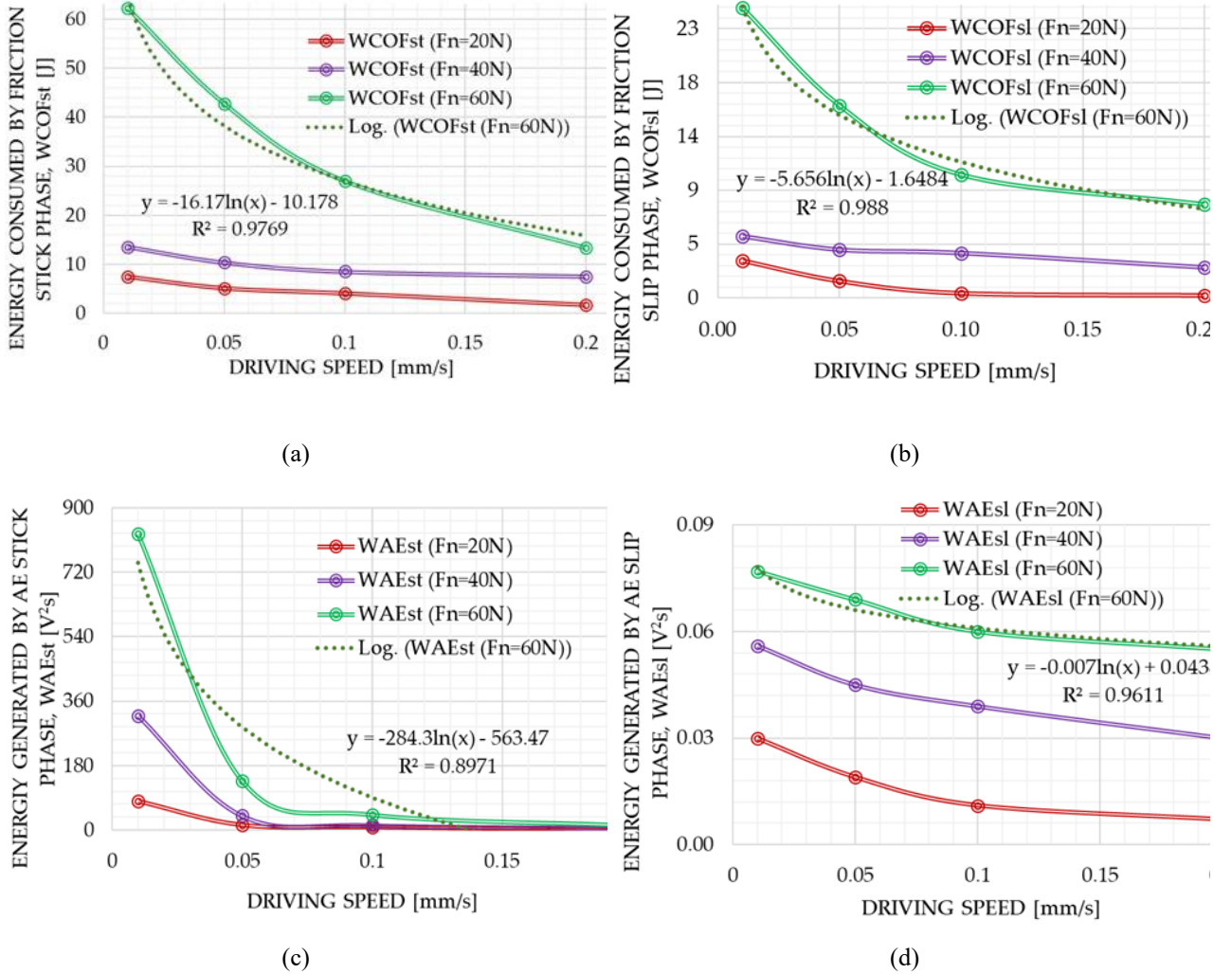
Fig. 4.10. Variation in energies with different driving speeds (mm/s): (a) energy consumed by friction in slip phase, W_{COFsl} (J), (b) energy consumed by friction in stick phase, W_{COFst}(J), (c) energy generated by AE in slip phase, W_{AEsl} (V^{2}s), (d) energy generated by AE in stick phase, W_{AEst}(V^{2}s).

At very low-speed regimes, the characteristics of unlubricated friction between the cylinder and plane are essentially independent of the material properties(C. Caroli, P. Noziers, 1995; E. Rabinowicz, 1958). The analysis of slip oscillations in the stick-slip phenomenon considered the kinetic friction coefficient as a function of driving speed and the static friction coefficient as a function of stick time. The results of studies, including notable references such as *(Heslot F., 1994;*

Baumberger T., 1996; Caroli C., and Noziers P., 1995; and Baumberger et al., 1995), highlight a clear logarithmic relationship between the static friction coefficient and the stick time (t_{stick}) of the form $\mu_s(t) = a_s + b_s \ln\left(\dfrac{t}{t_0}\right)$ with t_0 being an arbitrary normalisation constant; thus μ_s depends on the history of the interaction and the conditions to which the surfaces were previously subjected. This suggests that the static friction coefficient μs is not just an instantaneous property but is influenced by the "memory" of the material or the history of contact and deformation. The static dependence of COF on stick time (t_{stick}) can be seen in Fig. 4.12.
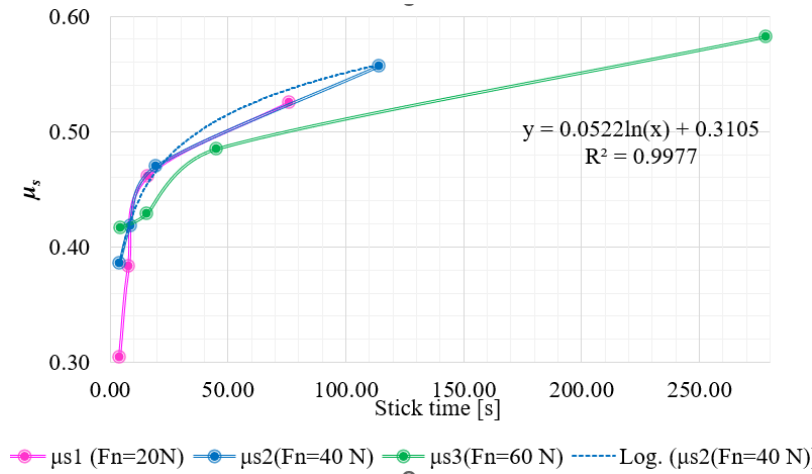

Fig. 4.12. The stick time and normal force influence the static friction coefficients.

As observed in Fig. 4.12, μ_s gradually increases with the duration of the stationary contact before the initiation of movement. This response describes how microscopic interactions at the surface level significantly influence the stick-slip phenomenon in cylinder-plane contact. Hertz's theory suggests that small contact areas under concentrated pressure lead to elastic deformation, increasing adhesion force and static friction. Surface-level processes like diffusion, adsorption, and chemical reactions further amplify this. The dynamic friction coefficient (μ_k) varies with sliding speed: it decreases logarithmically at low speeds and increases at higher speeds, indicating a shift to a new dissipation regime. This transition from a "slow flow" regime to one dominated by sliding inertia is captured in works by Rabinowicz (1965), Ruina A. L. (1983), and Rice J. R. (1983). They propose a characteristic length, L_{mc}, that encapsulates this transition.

In this context, a characteristic length Lmc can be defined, such that:

$$\mu_k\left(\frac{v}{v_0}\right) = a_k - b_k \ln\left(\frac{v}{v_0}\right) \; ; \; \mu_k\left(\frac{v}{v_0}\right) = \mu_s\left(\frac{t}{t_0}\right) = \mu_s\left(\frac{L_{mc}}{v}\right). \qquad (4.1)$$

Where, v_0 is an arbitrary normalising constant.

In studying friction and sliding behaviour in Hertzian contact, L_{mc} serves as an essential parameter, reflecting the "memory" or "age" of microscopic interactions. Moreover, L_{mc} is directly

associated with the duration of time during which the contacting surfaces remain in a state of adhesion, known as "stick time," and can be interpreted as the average displacement necessary to renew or "reset" the population of micro-contacts, thereby marking a transition between sets of contacts at the microscopic level (Dieterich J. H., 1994). The static friction coefficients obtained experimentally at a speed of 10^{-4} mm/s were compared and validated with those determined by the fractal method, as detailed in Chapter 3, with the results found in Table 4.2.

Table 4.1. Comparison of static friction coefficients
from experimental method against the fractal method.

Driving Speed (mm/s)	F_n= 20 N			F_n = 40 N			F_n = 60 N		
	μ_{s1}*	μ_{sf1}**	Relative error [%]	μ_{s2}*	μ_{sf2}**	Relative error[%]	μ_{s3}*	μ_{sf3}*	Relative error [%]
0.0001	0.751	0.749	0.267	0.813	0.816	0.369	0.851	0.856	0.587

* Static friction coefficients. ** Static friction coefficients from fractals.

Chapter 5

Conclusions and further work

In this chapter, the summary of the main findings of the thesis is presented. Moreover, various recommendations for future research on the topic are proposed.

5.1. Thesis conclusions

To begin with, techniques of fractal modelling were employed to depict the roughness characteristics of the rails at the Făurei Test Centre in Romania. Both the structure function and the Weierstrass-Mandelbrot function were used to capture the intricate nature of the rail roughness effectively. The analysis assessed 41 conventional statistical parameters and compared them with the rail acoustic roughness obtained from measurements and the simulated fractal parameters.

Four sections of rail roughness testing, each of 7.5 meters, were systematically evaluated and segmented from 1 m to 7.5 meters. A comparison was made between the statistical parameters of the experimental measurements and the parameters simulated using the W-M function, revealing that a representative number of these parameters fell within a relative error of 10%. However, it was observed that the fit of the number of simulated parameters to the measured parameters decreased as the measurement length decreased.

Specifically, when amplitude, spatial, and hybrid parameters were considered for a measured roughness of 7.5 m, their correspondence to the simulated roughness at the same length was found to be 100%. But as the measured length decreased, the matching of the number of parameters was noted to decrease gradually to 66.6% for a distance of 2.5 m and then to 50% for a length of 1 m.

For a measured roughness of 30 m, the roughness parameters from the experimental measurements were found to match the simulated parameters by 83.33% for the same length. As the measurement length increased, both the measured and simulated roughness profiles were observed to have almost symmetrical Gaussian distributions.

Parameters such as ADF, ACF, PSD, and BAC exhibited close roughness equivalence when simulated with the W-M function. The convergence of experimental measurements and simulated profiles underscored the effectiveness of the fractal approach in decrypting the complex behaviour of rail roughness.

Continuing, fractal modelling techniques were employed to assess the static friction coefficient within the context of Hertzian wheel-rail contact mechanics, with surface roughness taken into

consideration. The fractal parameters D and G_{fs} were directly found to influence the elastic regime, affecting the critical contact area, the critical deformation, and the elastic contact force.

The transition between the elastic and elastoplastic regimes was characterised by the fractal parameters D and G_{fs}, which were found to influence the surface roughness and the interactions between asperities. When the material reached its fully plastic state, substantial deformations in the asperities were observed, diminishing the importance of the initial surface characteristics and fractal parameters.

Regarding the total contact force, significant impacts on the elastic and elastoplastic regimes by variations in fractal parameters D and G_{fs} were identified, but no effect on the fully plastic regime was observed. In the context of Hertzian wheel-rail contact, the fractal parameter D was noted to influence the real contact area and the maximum spot size, indirectly affecting acoustic emissions and noise generation.

The total normal load was found to interact with the fractal parameter D, especially within the range of 1.4-1.8. The static friction coefficient was influenced by factors such as the maximum spot area, the scale factor G_{fs}, the applied force, and the fractal parameter D. Variations in D. G_{fs} were observed to influence the static friction coefficient between 1.4 and 1.9. Still, outside this range, it was noted that it might be overshadowed by specific surface interactions or insufficient asperity contact.

These observations underscore the importance of understanding and considering these parameters when surface interactions are assessed.

In the concluding phase of the research, the stick-slip phenomenon for Hertzian contact was closely examined.

Acoustic emission signals generated during the relative motion of cylinder–plane specimens were captured by a multipurpose acquisition system and were processed using basic parameters based on the RMS signal. The objective was to determine if the onset and sensitivity of the stick-slip phenomenon could be detected and predicted through the acquisition and analysis of AE using equipment and software with low requirements. Tests were conducted under various conditions, including normal loads and sliding speeds. Although the tests were not exhaustive, they confirmed the feasibility of using non-complex AE parameters as a non-destructive method for detecting the stick-slip phenomenon.

In all tests conducted, the presence of the stick-slip phenomenon was confirmed by the variation in the coefficient of friction and its coincidence with AE bursts. Significant influences on the coefficient of friction were found to be the driving speed, sliding speed, and normal load. Greater normal loads and slower driving speeds were found to increase the sliding velocity.

Regarding acoustic emissions, a reduced AE activity was observed during the stick phase, while high amplitude bursts of activity were presented during the sliding phase. The presence of the stick-slip phenomenon was detected by measuring the amplitude and energies of the acoustic emission, which were evidenced by a strong positive correlation between them.

Amplitudes and energies generated by the acoustic emission were found to be significant and confirmed a direct dependence on the stick-slip phenomenon for non-lubricated Hertzian linear contact. Thus, the acoustic emission detected through parameter analysis was identified as an essential indicator for detecting and monitoring the stick-slip phenomenon.

From another perspective, the analysis of the experiments highlighted that a static friction coefficient (COF) was derived from the stick-slip phenomenon. This was perceived as a reflection of the specific behaviour of the material pair under certain conditions. Furthermore, a COF corresponding to the saturated regime was deduced using statistical methods. When compared with the COF obtained through fractal modelling, the coherence and relevance of using fractal theory in assessing and predicting the friction behaviour of materials in contact were demonstrated. The conclusion is that acoustic emission, coupled with fractal modelling, provides a robust and effective framework for studying and understanding the stick-slip phenomenon and its associated friction properties.

5.2.   Contributions

- Analysis of the running surface quality of the railway track, focusing on the specific fractal dimensions of the roughness of the rails and the driving wheels, employing fractal geometry, and deducing the unique fractal parameters D and Gf, which are independent of the measurement scale;

- The utility of the Weierstrass-Mandelbrot function for simulating roughness height is argued by comparing it with 41 classical roughness measurement parameters, emphasising the relevance of fractal dimensions of surfaces for Hertzian Contact;

- Establishing the minimum length for measuring rail roughness, ensuring that the results are conclusive and aligned with international standards on acoustic roughness (EN 15610: 2019), reflecting the fractal dimensions of roughness;

- The experimental determination of the static friction coefficient for Hertzian contact, followed by its validation through the application of a theoretical model employing fractal approaches.

- Detecting Acoustic Emissions (AE) as a crucial indicator and an effective non-destructive method for identifying and monitoring the stick-slip (SS) phenomenon in non-lubricated linear Hertzian contacts. Utilising AE allows for direct and instantaneous observation of

transitions between stick and slip phases, thus providing deep insights into the dynamics of friction and surface interactions.

- Defining the memory length as a determining factor for the static friction coefficient in relation to stick time and determining the critical speed of transition between the stick and slip phases;

5.3. Recommendations and future work

Diagnosing rail degradation and the stick-slip phenomenon using AE transducers.

Diagnosing rail degradation and capturing the stick-slip phenomenon using AE transducers. Utilising AE transducers allows for accurate detection and real-time monitoring of rail degradation and captures the intricacies of the stick-slip phenomenon. This deeper insight facilitates more efficient interventions and enhanced infrastructure maintenance management.

Linking various wear patterns of rails and wheels with changes in fractal dimensions.

By conducting a detailed examination and modelling using the fractal method of different wear patterns, we can gain a clearer insight into how these wear patterns influence fractal dimensions and, consequently, the dynamic behaviour of rails and wheels. Understanding this relationship can pave the way for devising more efficient strategies for preventing and repairing rail and wheel degradation.

Suggestions for implementing fractal dimensions in the standardised characterisation of acoustic roughness.

Incorporating fractal dimensions as a standard in the analysis of acoustic roughness could provide a more coherent metric for assessing the performance of rails and wheels. This might also facilitate data communication and comparison across different studies and applications.

Highlighting the influence of fractal parameters of the equivalent roughness of rails and wheels on vertical rolling vibrations.

By assessing the stiffness of Hertzian surfaces with fractal roughness, we can gain crucial insights into how changes in fractal parameters impact vertical vibrations. This knowledge is essential, as the interplay of fractal roughness parameters, contact dynamics, load distribution, and material properties jointly influence these vibrations. Understanding these interactions could lead to developing solutions for vibration reduction and prolonging the lifespan of rails and wheels.

Establishing a method to evaluate unique fractal parameters using surface probing devices with varying resolutions.

This method could offer a more detailed and nuanced surface examination, accurately revealing roughness variations and structure. Additionally, it might enhance the accuracy and reliability of measurements and provide a framework for verifying acoustic roughness results. In the context of

railway maintenance, this approach could be pivotal for drafting a strategic maintenance plan. With the ability to precisely anticipate roughness variations and fractal parameters, the optimal timing for rail rectification could be determined, ensuring efficient operation and prolonging the life span of the railway infrastructure.

References

[1]   Baumberger et al., Nonlinear analysis of stick-slip bifurcation in the cree-controlled regime of dry friction, Physical Review E, 51(5), 1995, pp. 4005-4010.

[2]   Benabdallah H. S., Aguilar D. A., Acoustic Emission and its Relationship with Friction and wear for Sliding Contact. Tribol. Trans., 2008, 51, 738 - 747.

[3]   Berry M. V. and Lewis Z. V., On the Weierstrass - Mandelbrot fractal function, Proc. R. Soc. Lond. A, 370, 1980, 459 - 484.

[4]   Bhushan B., Majumdar A., Elastic-plastic contact model for bifractal surfaces, Wear, 153, 1992, 53 - 64.

[5]   Caroli C., Nozieres P., Persson B. N. J., Tossatti E., Dry friction as a hysteretic elastic response. In Physics of Sliding Friction, Springer: Dordrecht, The Netherlands, 1995, pp. 27 - 49.

[6]   Chang W. R., Etsion I., Bogy B. D., An elastic-plastic model for the contact of rough surfaces. ASME J. Tribol., 1987, 109, 257 - 263.

[7]   Chang W. R., Etsion I., Bogy D. B., Static friction coefficient model for metallic rough surfaces. ASME J. Tribol., 1988, 110, 57 - 63.

[8]   Diehl R. J., Holm P., Roughness measurement-have the necessities changed?, Journal of Sound and Vibrations, 293, (2006), 777 - 783.

[9]   Eid H., Adams G. G., McGruer N. E., Fortini A., Buldyrev S., Srolovitz D., A Combined Molecular Dynamics and Finite Element Analysis of Contact and Adhesion of a Rough Sphere and a Flat Surface. Tribol. Trans., 2011, 54, 920 - 928. https://doi.org/10.1080/10402004.2011.615638.

[10]   Esveld C, Modern Railway Track, MRT-Productions, 2001, Chap 2.

[11]   Gadelmawla E. S. et al., Roughness parameters, J. Mater. Process. Technol, 123, 2002, 133 - 145.

[12]   Ganti S., Bhushan B., Generalised fractal analysis and its surfaces applications to engineering surfaces, Wear, 180, 1995, 17 - 34.

[13]   Green I., Exact Spectral Moments and Differentiability of the Weierstrass-Mandelbrot Fractal Function, J. Tribol., 142(4), 2020, 041501.

[14]   He L. and Zhu J., The fractal character of processed metal surfaces, Wear, 208, 1997, 17 - 24.

[15]   He P. et al., Analysis of the best roughness surface based on the bearing area curve theory, Proc IMechE Part J: J Engineering Tribology ,2021, 1 - 14.

References

[16]   Heslot F., Baumberger T., Perrin B., Creep, stick-slip, and dry-friction dynamics: Experiments and a heuristic model. Am. Phys. Soc., 1994, 49, 4973 - 4950.

[17]   Johnson K. L., Contact mechanics [M]. Cambridge: Cambridge University Press, 1987.

[18]   Kogut L., Etsion I., A semi-analytical solution for the sliding inception of a spherical contact. ASME J. Tribol., 2003, 125, 499 - 506.

[19]   Kogut L., Etsion I., A static friction model for elastic-plastic contacting rough surfaces. ASME J. Tribol., 2004, 126, 34 - 40.

[20]   Kogut L., Etsion I., Elastic–plastic contact analysis of a sphere and a rigid flat. ASME J. Appl. Mech., 2002, 69, 657 - 662.

[21]   Lontin K., Khan M., Interdependence of friction, wear, and noise. Friction, 2021, 9, 1319 - 1345. https://doi.org/10.1007/s40544-021-0500-x.

[22]   Majumdar A. and Bhushan B., Role of fractal geometry in roughness characterisation and contact mechanics of surfaces, J. Tribol., 112, 1990, 205 - 216.

[23]   Majumdar A., Bhushan B., Fractal model of elastic–plastic contact between rough surfaces. ASME J. Tribol., 1991, 113, 1 - 11.

[24]   Majumdar A., Bhushan B., Fractal model of elastoplastic contact between rough surfaces, J. Tribol. 113, 1991, 1 - 11.

[25]   Majumdar A., Bhushan B., Role of fractal geometry in roughness characterisation and contact mechanics of surfaces J, Journal of Tribology, 1990, 112(2): 205 - 216.

[26]   Majumdar A., Tien C. L., Fractal characterisation and simulation of rough surfaces, Wear, 136, 1990, 313–327.

[27]   Majumdar A., Tien C. L., Fractal Network Model for Contact Conductance, J. Heat Transfer., 113 (3), 1991, 516 - 525.

[28]   Mandelbrot B. B., Self-affine fractals and fractal dimension, Phys. Scr. 32, 1985, 257 - 260.

[29]   Mandelbrot B. B., The Fractal Geometry of Nature, eds. Echo Point Books & Media, (Brattleboro, Vermont, 2021.

[30]   Mulakaluri N., Persson B. N. J., Adhesion between elastic solids with randomly rough surfaces: Comparison of analytical theory with molecular-dynamics simulations. EPL 2011, 96, 66003. https://doi.org/10.1209/0295-5075/96/66003.

[31]   Nayak P. R., Some aspects of surface roughness, Wear, 26, 1973, 165 - 174.

[32]   Otero Yugat J., Contribución al estudio de las vibraciones producidas por el contacto rueda-carril y su transmisión al entorno, M. S. thesis, Universitat Politècnica De Catalunya, 2009.

[33]   Ozaki S., Matsuura T., Maegawa S., Rate, state and pressure-dependent friction model based on the elastoplastic theory. Friction, 2020, 8, 768 - 783.

References

---

[34]   Persson B. N. J., Sliding Friction. In Physical Principles and Applications, Springer-Verlag: New York, NY, USA, 2000.

[35]   Persson B. N. J., Tossati E., Physics of sliding friction, 1995, Series E, Applied Science, 311.

[36]   Popov V. L., Contact Mechanics and Friction, Physical Principles and Applications, Springer, 2009.

[37]   Singh A. N., The theory and construction of non-differentiable functions, in Squaring the Circle and Other Monographs, Chelsea Publishing, 1953.

[38]   Thomas T. R., Thomas A. P., Fractals and engineering surface roughness, Surf. Topogr., 1, 1988, 1 - 10.

[39]   Thompson D. J., Railway Noise and Vibration: Mechanisms, Modelling and Means of Control. Elsevier Ltd, 2009,

[40]   Thompson D. J., The influence of the contact zone on the excitation of wheel/rail noise, Journal of Sound and Vibrations, 267 (2003) 523 - 536.

[41]   Verheijen E., A survey on roughness measurements, Journal of Sound and Vibrations, 293 (2006), 784 - 794.

[42]   Villamarin R. A., A model for railway induced ground vibrations in the frame of preliminary assessment studies, M. S. thesis, Universitat Politècnica De Catalunya, 2011.

[43]   You J. M., Chen T. N., A static friction model for the contact of fractal surfaces, Proc. IMechE Vol. 224 Part J: J. Engineering Tribology, 2010, pg. 513 - 518, DOI: 10.1243/13506501JET760

[44]   Yuan Y., Gan L., Liu K., & Yang X., 2016. Elastoplastic contact mechanics model of rough surface based on fractal theory. Chinese Journal of Mechanical Engineering, 30(1), 207 - 215.

[45]   Zhang C. et al., Static friction coefficient model of joint surface based on the modified fractal model and experimental investigation, The International Journal of Advanced Manufacturing Technology, 2022, 124 (11-12), 1 - 15

[46]   Zhang W. et. al., Wheel / rail adhesion and analysis by using scale roller rig, Wear, 253, (2002), 82 - 88.

[47]   Zhang X., Xu Y. and Jackson R. L., An analysis of generated fractal and measured rough surfaces in regards to their multi-scale structure and fractal dimension, Tribol. Int., 105, 2017, 94 - 101.

[48]   Zhang Y., Zhang X., Jiang L., et al. Fractal Model of Static Frictional Coefficient on Joint Surface Considering Elastic-plastic Deformation. Journal of Taiyuan University of Science and Technology of China, 2014, 25(4): 294 - 301.

[49]   Zhao B., Xu H. & Lu X., 2019. Sliding Interaction for Coated Asperity with Power-Law Hardening Elastic-Plastic Coatings. Materials, 12(15), 2388.

References

[50]   Zhao Y. W., Maietta D. M., L. Chang, An asperity micro-contact model incorporating the transition from elastic deformation to fully plastic flow. ASME J. Tribol., 2000, 122, 86 - 93.

[51]   Zhou G. Y. et al., Fractal geometry model for wear prediction, Wear, 170, 1993, 1 - 14

[52]   Zhou G. Y., Leu M. C., Blackmore D., Fractal geometry model for wear prediction. Wear, 1993, 170, 1 - 14.

[53]   Zhou G., Statistical, random and fractal characterisations of surface topography with engineering application, A Dissertation Submitted to the Faculty of New Jersey Institute of Technology in Partial Fulfilment of the Requirements for the Degree of Doctor of Philosophy Department of Mechanical and Industrial Engineering, 1993.

*   EN ISO 21920 - 2: 2023 Geometrical product specifications (GPS) - Surface texture: Profile - Part 2: Terms, definitions and surface texture parameters.

**   EN 15610: 2018 Railway applications. Acoustics. Rail and wheel roughness measurement related to noise generation.

*** ISO 3095: 2013 Acoustics - Railway applications - Measurement of noise emitted by rail bound vehicles.